universität wien

MASTERARBEIT / MASTER'S THESIS

Titel der Masterarbeit / Title of the Master's Thesis

„Self-Assembly of Hollow Colloidal Silica Cubes“

verfasst von / submitted by

Margaret Rosenberg

angestrebter akademischer Grad / in partial fulfilment of the requirements for the degree of

Master of Science (MSc)

Wien, 2019 / Vienna, 2019

Studienkennzahl lt. Studienblatt / degree programme code as it appears on the student record sheet:	A 066 910
Dissertationsgebiet lt. Studienblatt / field of study as it appears on the student record sheet:	Masterstudium Computational Science
Betreut von / Supervisor:	Ass.-Prof. Dr. Sofia S. Kantorovich, Privatdoz

Abstract

Among the multitude of recently synthesized non-spherical colloids, hollow silica cubes distinguish themselves by their charged surface and by the strong influence of Van der Waals forces on their behaviour. Depending on the choice of solvent, they self-assemble into intriguingly anisotropic structures or remain colloidally stable[1]. Despite extensive experimental work done on this topic, there exists neither a detailed theoretical explanation, nor a characterization of the behavior of the colloids in such systems.

By adapting the superball model used to study similarly-shaped colloids[2], we examine the influence of the suspension medium on the electrostatic forces affecting the colloids. We begin by investigating a single colloid, showing how the cubic shape leads to asymmetry in the counterion distribution near the surface. To understand the interactions of pairs of cubes, we measure the effective potential of mean force between them. This shows a clear influence of the anisometric shape, which gives rise to the hitherto unexplained attachment mechanism observed in experiment[3].

This work shows how the interplay of tuneable factors such as the shape of the cubes, the choice of solvent and the salinity thereof significantly impact the behavior of the colloids by tipping the delicate balance between Van der Waals attraction and electrostatic repulsion. Moreover, we shed light on the process of self-assembly that gives rise to the microstructures seen in experiment. In conclusion, we obtain a comprehensive understanding of the behavior observed in these systems, paving the way for future applications.

Zusammenfassung

Von der Vielfalt an letztlich synthetisierten kolloidalen Suspensionen heben sich hohle Siliciumdioxidwürfel sowohl durch ihre geladene Oberfläche als auch durch den starken Einfluss von Van der Waals Kräften auf ihre Verhalten ab. Je nach Wahl der Trägerflüssigkeit schließen sie sich zu asymmetrischen Strukturen zusammen (self-assembly) oder bilden eine stabile kolloidale Suspension[1]. Obwohl solche Systeme experimentell bereits gründlich untersucht worden sind, gibt es noch keine ausreichende theoretische Erklärung für das Verhalten der Kolloide oder Charakterisierung davon.

Durch Erweiterung des bereits für ähnlich geformte Kolloide verwendeten superball Modells[2] werden die Auswirkungen der Trägerflüssigkeit auf die elektrostatischen Kräfte, welche die Kolloide beeinflussen, untersucht. Von einem einzigen Kolloid ausgehend wird zunächst gezeigt, wie die kubische Form zu einer Asymmetrie in der Verteilung der Gegenionen in der Nähe der Oberfläche des Kolloids führt. Um die Wechselwirkung zwischen Paaren von Würfeln zu verstehen wird das Potential zwischen ihnen gemessen, dies zeigt einen deutlichen Einfluss der nicht isometrischen Form, wodurch der experimentell beobachtete, aber bisher unerklärte „attachment-Mechanismus“ entsteht[3].

Diese Arbeit zeigt wie das Zusammenspiel von kontrollierbaren Faktoren wie die Form der Würfel, die Trägerflüssigkeit und der Salzgehalt der Trägerflüssigkeit das Verhalten der Kolloide stark beinflusst, indem das empfindliche Gleichgewicht zwischen Van der Waals Anziehung und elektrostatischer Abstoßung gekippt wird. Weiters wird der Prozess der self-assembly, der zu den experimentell beobachteten Mikrostrukturen führt, beleuchtet. Zusammenfassend wird eine ausführliche Erklärung für das in den Systemen beobachtete Verhalten geboten, und so der Weg für zunkünftige Anwendungen geöffnet.

Acknowledgements

I owe a profound debt of gratitude to (now Dr.) Joe Donaldson, who provided countless hours of mentoring and served as a co-supervisor in all but name. I'd also like to thank my supervisor Dr. Sofia Kantorovich for her guidance and insights, and the Dipolar Soft Matter group for their support. In addition, I greatly benefited from helpful discussions with Prof. Ivanov and Prof. Philipse on electrostatics and on cube behavior, respectively. Last but in no way least, I thank my friends, family and boyfriend for their love and support.

Contents

1 | Introduction

1.1 Colloidal Physics

A colloidal suspension is a system composed of two immiscible phases: microscopic particles (colloids) and a continuous carrier medium in which they are dispersed. While this thesis focuses on the specific example of nanoscale silica particles suspended in a liquid solvent, typically water or ethanol, colloidal systems span almost every combination of phases (except gas in gas), with particle sizes ranging from $1nm$ to $50\mu m$.[4] This makes them abundant in nature, from fog to ink to (ice) cream, and gives rise to a flexibility which suggests a multitude of applications in fields such as medicine[5] or food science[6], provided they can be properly understood and characterised.

At the microscopic level, a charged colloidal system is governed by a competition between Van der Waals attraction and electrostatic repulsion. This may either create a stable dispersion of the particles or result in self-assembly into structures such as lattices. Due to the small length scale, the colloids also exhibit significant Brownian motion. For simple particle geometries, i.e. spheres, these systems have already been extensively studied and are well-described[7,8].

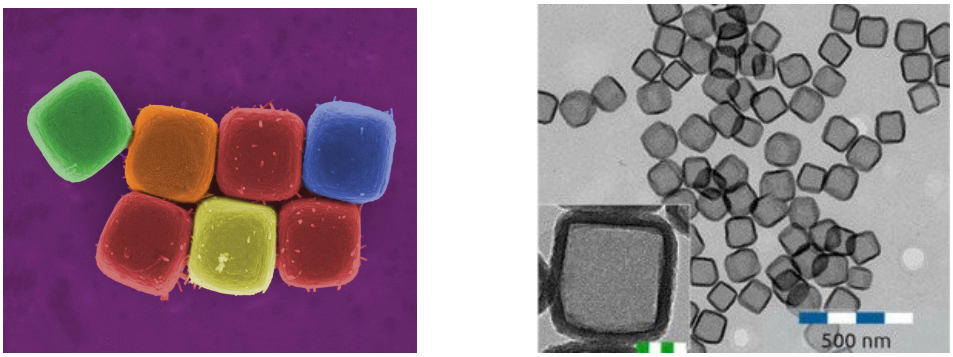

Figure 1.1: Left: A 2011 cover of Soft Matter[9] featuring colloidal cubes. Right: experimental image of hollow colloidal silica cubes.[1]

However, colloidal particles exhibit a variety of anisotropic shapes even in nature, such as the rods common in liquid crystals. Additionally, an increasing amount of anisometric colloids are being created via synthesis, including the cubes shown in Figure 1.1[1,9]. In previous investigations of cubical particles, the difference in shape has been shown to affect the behavior of the particles in solution[2], and in cases of assembly, the structures formed[10,11]. Still, due to the high complexity of the systems involved, rigorous investigations of these suspensions remain in their infancy.

This thesis goes beyond such boundaries by obtaining a pair potential that can describe the interactions of charged colloidal cubes. The suspension to be investigated consists of nanoscale hollow silica cubes with rough surfaces, which show self-assembly despite their like-charged surfaces[3,9], seemingly favoring certain orientations, and form anisotropic structures contrary to the established theory for spheres[7]. As an analytical solution would - among other challenges - imply solving the

many-body problem, this work uses molecular dynamics simulations based on experimental observations and parameters[3,12] to recreate the system in silico. Thus properties such as counterion densities, field strengths and orientation-dependant potentials can be computed and compared to theory and experiment. Furthermore, we will explore possibilities to reconfigure the system by tuneing properties such as solvent and salinity. By clarifying the attachment mechanism and pair potential of these cubes, we lay the foundation for further study of the resulting structures.

1.2 Thesis Outline

This thesis is split into four chapters, which are further subdivided according to topic:

- Theory and Methods: contains a brief review of the theoretical and computational framework
- The system in silico: deals with the translation of experimental parameters into a simulation model
- Electrostatics of a single cube: describes the electric double layer and, generally, the field around such a cube
- Pairwise interactions: explores the pair potential of cubes and explains their assembly mechanism

Lastly, the outlook summarizes the results achieved and suggests future work.

2 | Theory and Techniques

The nature of colloidal systems lends itself to a model in which the carrier medium is modelled implicitly via a continuum approach, and the colloids are represented explicitly, using a coarse-grained approach. The necessary theory for such a mixed model pertinent to the experimental system presented in the introduction is sketched here, followed by an overview of the standard computational methods necessary to reproduce and investigate it.

2.1 Theory

To draw up our simulation model, we require a characterization of the colloids to derive their coarse-grained representation, and the interaction potentials necessary to describe the mechanics of the system. We achieve the latter by considering the forces acting on any simulation particle, using the approach outlined in Israelachvili[13] of separating them into three categories based on their origin: entropic, electromagnetic or quantum mechanical. As forces of entropic origin lie outside the scope of this thesis, we will instead conclude the section with Brownian motion.

2.1.1 Anisometric Colloids

Although the colloids featured in this thesis are commonly referred to as "cubes", a more precise description of their shape is given by the superball equation with the shape parameter q:

$$\left|\frac{x}{r}\right|^{2q} + \left|\frac{y}{r}\right|^{2q} + \left|\frac{z}{r}\right|^{2q} \leq 1\,. \tag{2.1}$$

Here r corresponds to the radius of a sphere, or half the height of a cube. For the limit of $q \to 1$, the equation reverts to that of a sphere, whereas the limit $q \to \infty$ becomes a perfect cube. This allows us to quantify the asphericity of these colloids, as shown in Figure 2.1.

2.1.2 Forces of Quantum Mechanical Origin

2.1.2.a Van der Waals Forces

The term Van der Waals forces describes the sum of three attractive dipole-dipole interactions that occur even in electrically neutral molecules[15]. These are the Keesom interaction between permanent dipoles, the Debye interaction between permanent and induced dipoles and the London dispersion interaction between transient dipoles. All three of their free energies scale as $-r^{-6}$, where r is the center to center distance between molecules, which allows us to write the molecular

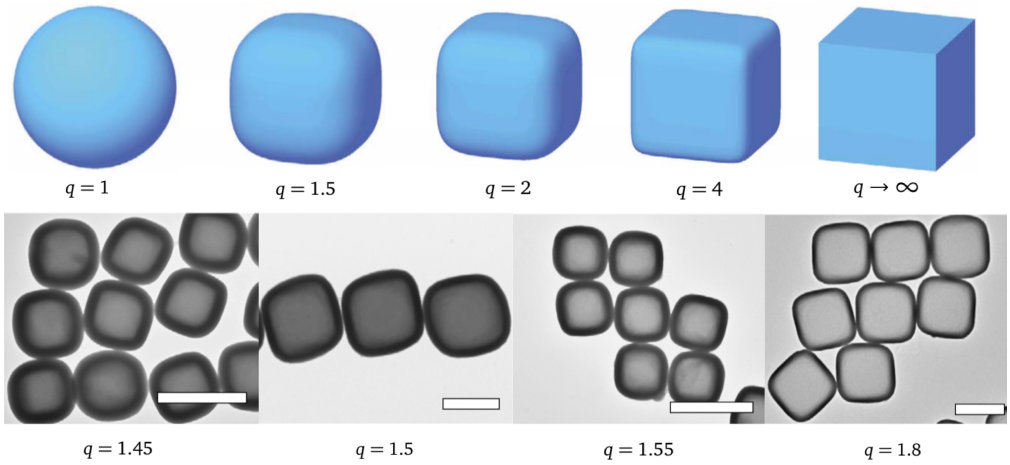

Figure 2.1: A comparison of the analytical model to TEM images of hollow silica superballs, adapted from[14]

potential corresponding to these forces as:

$$U_m(r) = -\frac{C_{1,2}}{r^6}\,, \tag{2.2}$$

where $C_{1,2}$ is a constant that depends on the interacting molecules 1 and 2. At the macroscopic scale of colloids, the interaction depends on the shape and material of the interacting particles. Assuming pairwise additivity, we can derive a formulation consisting of a material-dependent factor called the Hamaker constant, and a geometrical factor[16]. The Hamaker constant of the Van der Waals interaction potential of particle 1 with density ρ_1 and particle 2 with density ρ_2 is given by:

$$A_{12} = \pi^2\,\rho_1\,\rho_2\,C_{1,2}\,. \tag{2.3}$$

The geometric factor is a double volume integral that has been computed for geometries such as spheres[17] and cubes[16]. The attraction potentials for either two spheres of radius a or two solid cubes of length l are:

$$U_{SS}(r) = -\frac{A_{12}}{6}\left(\frac{2a^2}{r^2-4a^2} + \frac{2a^2}{r^2} + \log\left(\frac{r^2-4a^2}{r^2}\right)\right)\,; \tag{2.4}$$

$$U_{CC}(r) = -\frac{A_{12}l^2}{12\pi}\left(\frac{1}{r^2} + \frac{1}{(d+2l)^2} - \frac{2}{(d+l)^2}\right)\,. \tag{2.5}$$

We see that the differences in shape do affect the pair potential. These expressions are still lacking two important considerations. For one, we are overestimating the strength of the London dispersion interaction. Since electromagnetic fields take a finite time to propagate, the fluctuating dipoles

are less correlated and so the power law is closer to r^{-7} at certain length scales. This is called the retardation or Casimir-Polder effect[16].

The strength of the interaction is also influenced by the electrostatic properties of the medium across which the particles are interacting. These effects can be taken into consideration by modifying the Hamaker constant. This is described by Lifshitz theory, which gives an analytical expression for the Hamaker constant of a pairwise interaction across a medium using the main electronic absorption frequency, dielectric constants and refractive indices of the surrounding and interacting media[13]. For commonly used media, it is also often possible to find experimental measurements of the Hamaker constant[18]. Finally, in the case where a Hamaker constant is entirely unknown, the combining relations offer a method to obtain an approximation using other known Hamaker constants. For the specific case of two particles, both of a medium with the Hamaker constant A_{11}, interacting across a medium with the Hamaker constant A_{33}, the Hamaker constant of the total interaction can be approximated by:

$$A_{131} = \left(\sqrt{A_{11}} - \sqrt{A_{33}}\right)^2 ; \tag{2.6}$$

provided that the dielectric constant of the surrounding medium is not too high.[13]

2.1.2.b Steric Repulsion

Our current model would have any two molecules with some attractive force between them move towards each-other until they occupy the exact same position, which is obviously inaccurate. When two molecules approach too closely, their electron clouds overlap, which creates a strong repulsion. This steric interaction is most simply modelled by the hard-sphere potential, which is infinitely large in the case of overlap and zero otherwise. As this would not be computationally stable, even if it were made feasible by choosing very large finite repulsion, we choose the softer approximation of $U_S(r) = \frac{B}{r^{12}}$, where B is constant that remains to be chosen. The shape of this potential was chosen primarily for computational efficiency- we will see that it is the square of the attractive force term- and does not have a theoretical background other than expediency.

2.1.2.c Lennard-Jones and Weeks-Chandler-Anderson Potentials

Moving towards simulation, we begin by combining the attractive and repulsive molecular potentials described above into the Lennard-Jones pair potential. For spherically symmetric particles with a diameter of σ, the total pair potential is given by:

$$U_{LJ}(r) = \frac{B}{r^{12}} - \frac{C_{1,2}}{r^6} = 4\epsilon\left[\left(\frac{\sigma}{r}\right)^{12} - \left(\frac{\sigma}{r}\right)^6\right]. \tag{2.7}$$

The prefactor 4 ensures that the parameter ϵ is precisely the well depth, i.e. the maximal value of the attraction. This sets the energy scale for the interaction, just as σ defines the length scale. Should the particles have different diameters, the length parameter can be calculated by using the Lorentz(-Berthelot) rules $\sigma_{ij} = \frac{1}{2}(\sigma_{ii} + \sigma_{jj})$. To avoid computing additional interactions too weak to be significant, the potential is also set to zero past a certain distance cutoff, conventionally 2.5σ. However, not all particles we will consider in simulation experience Van der Waals attraction. Ions, for instance, should only experience the steric repulsion aspect of the potential. To make it purely repulsive, we add ϵ to the Lennard Jones potential and truncate it at the former maximum, $r_m = 2^{\frac{1}{6}}\sigma$. The result is known as the Weeks-Chandler Anderson potential:

$$U_{WCA}(r) = \begin{cases} 4\epsilon\left[(\frac{\sigma}{r})^{12} - (\frac{\sigma}{r})^{6}\right] + \epsilon, & \text{if } r \leq 2^{\frac{1}{6}}\sigma \\ 0 & \text{else} \end{cases} . \tag{2.8}$$

As seen in the previous paragraphs, this potential is a simplification of the forces at play. However, it works remarkably well and is more computationally efficient than a detailed description.

2.1.3 Electrostatics

2.1.3.a Interactions between Charges

The basis for all interactions related to electrostatics in our model is Coulomb's Law:

$$U_C(r) = \frac{e^2}{4\pi\epsilon_0}\frac{q_1\, q_2}{r} . \tag{2.9}$$

Here q_1 and q_2 are the charge numbers of the particles, e is the elementary charge and ϵ_0 is the dielectric permittivity of vacuum. In this section, we modify the potential to be able to consider the effects of different solvents and salinities on the system. Any solvent we consider will "weaken" the Coulomb interaction between two charges relative to vacuum by a factor. This is known as the dielectric constant ϵ_r. Another way of describing this effect is by considering the Bjerrum length l_B, which gives the distance at which the electrostatic interaction between two charges is of the same magnitude as the thermal fluctuations in the system. Using the notation of k_B for the Bolzmann constant and T for the temperature, we can write the Bjerrum length as:

$$l_B = \frac{e^2}{4\pi\epsilon_0\epsilon_r k_B T} . \tag{2.10}$$

If the solvent we attempt to model contains salt, those ions also need to be considered in the electrostatic description of the system. Their influence was first described by Debye-Hückel theory[19]. The essence of what we need to consider to model our colloidal system is that each of the

ions in solution is on average surrounded by oppositely charged counterions. This results in the charge of each such ion being screened, which causes the potential of this interaction to decrease exponentially as the distance between the charges increases. To help quantify this effect, we first introduce the characterization for the concentration of salt in a solvent known as the ionic strength I. The ionic strength of a solution containing ion species i with charges q_i in concentrations c_i is given by[4]:

$$I = \frac{1}{2}\sum c_i q_i^2 \,. \tag{2.11}$$

With this measure, we can calculate the Debye length κ^{-1} which characterizes the strength of the screening described before

$$\kappa^{-1} = \sqrt{\frac{\epsilon_0 \epsilon_r k_B T}{2e^2 N_A I}} = \sqrt{\frac{1}{8\pi\, l_B N_A I}}\,, \tag{2.12}$$

where N_A is Avogadro's constant. Summarizing all the considerations of this section in a single electrostatic pair potential gives:

$$U(r)_{C-DH} = l_B k_B T\, \frac{q_1 q_2 \exp(-\kappa r)}{r}\,. \tag{2.13}$$

Aside from the charges in the distance, we now also see the influence of the dielectric as tuned by l_B, the screening as modified by κ and a factor of $k_B T$ which ties in to the thermal energy scale. In the limit $\kappa \to 0$, the expression reverts to the unscreened Coulomb potential.

2.1.3.b Charged Surfaces and the Electric Double Layer

In a liquid such as water or ethanol, a silica surface will dissociate protons from the surface silanol (SiOH) groups. This charge mechanism results in a negatively charged surface, with the charge density given by the dissociation constant K. To balance out this charge, the surface attracts counterions from the solvent. A certain amount of these counterions sit directly on the surface in what is called the Stern or Helmholz layer[13]. They may become transiently bound to it. Slightly further out, the remaining ions are distributed less densely in what is called the diffuse electric double layer. The total extent of both of these layers is equal to the Debye length κ^{-1} of the solution. Beyond it lies the bulk reservoir of ions and counterions of the liquid.

Figure 2.2 illustrates the arrangement of co-ions and counter-ions near an isolated surface. We will derive an analytic expression for the distribution of counterions in the diffuse layer for the "counterions-only" case. Since our experimental systems only contain monovalent ions, we will not consider the multivalent case except to warn that our observations here would require reformulation.

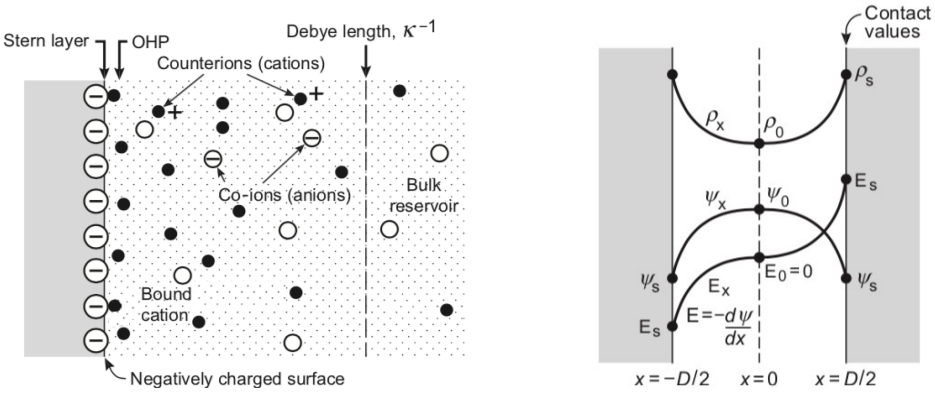

Figure 2.2: Left: Sketch of the ion distribution near a charged surface. OHP stands for Outer Helmholz Plane, which is the boundary between the Stern/Helmholz layer and diffuse layer. Right: a schematic drawing of the system used for the derivation of the counterion distribution. Both images are taken from[13].

Let ρ be the number density of ions and ψ be the electrostatic potential. To obtain better boundary conditions, we first consider the case of two charged surfaces separated by a distance D along the x-axis, then take the limit $D \to \infty$ to obtain ρ_x, the number density at distance x, near a single surface. We take $x = 0$ to be the midpoint between the two planes, and since only differences in potential will affect the behavior of the ions, set $\psi_0 = 0$. At equilibrium, the chemical potential μ of any counterion between these surfaces is[13]

$$\mu = e\psi + k_B T \log(\rho) \qquad \Rightarrow \qquad \rho = \rho_0 \exp\left(\frac{-e\psi}{k_B T}\right) . \tag{2.14}$$

The expression on the left gives rise to that on the right for the counterion density ρ by taking the exponential and some algebraic manipulation. We can combine it with the Poisson equation

$$\frac{d^2\psi}{dx^2} = -\frac{e\rho}{\epsilon_0 \epsilon_r} \tag{2.15}$$

to obtain the Poisson-Boltzmann equation

$$\frac{d^2\psi}{dx^2} = -\frac{-e\rho_0}{\epsilon_0 \epsilon_r} \exp\left(\frac{-e\psi}{k_B T}\right), \tag{2.16}$$

which gives the electrostatic potential at any point x when solved. That can further be used to calculate the density (Equation 2.14) and the electric field $\left(E = -\frac{d\psi}{dx}\right)$. Our focus, however, is to find a different expression for the number density, which we achieve by using the Poisson-Boltzmann equation to reformulate its derivative using the electric field:

$$\frac{d\rho}{dx} = \rho_0 \exp\left(\frac{-e\psi}{k_B T}\right)\frac{-e}{k_B T}\frac{d\psi}{dx} = \frac{\epsilon_0\epsilon_r}{k_B T}\frac{d^2\psi}{dx^2}\frac{d\psi}{dx} = \frac{\epsilon_0\epsilon_r}{2k_B T}\frac{d}{dx}\left(\frac{d\psi}{dx}\right)^2 ; \tag{2.17}$$

$$\rho_{x'} - \rho_0 = \int_0^{x'} \frac{d\rho(x)}{dx} dx = \frac{\epsilon_0 \epsilon_r}{2k_B T} \int_0^{x'} \frac{d}{dx} \left(\frac{d\psi}{dx} \right)^2 dx = \frac{\epsilon_0 \epsilon_r}{2k_B T} \left(\frac{d\psi}{dx} \right)^2 \Big|_{x'} \tag{2.18}$$

$$\rho_{x'} = \rho_0 + \frac{\epsilon_0 \epsilon_r}{2k_B T} \left(\frac{d\psi}{dx} \right)^2 \Big|_{x'} \tag{2.19}$$

This result gives an expression for the number density at any point x' for which we know the value of the field. In the limit of large separation between the surfaces, the midplane density ρ_0 goes to 0 and Equation 2.19 reduces to the term on the right. As a first result of these considerations, we can compute the density of counterions at one of the surfaces, that is $x = D/2$, the so-called "Contact value" of the number density. We still require an expression for the value of the field, which we obtain in a slightly roundabout way: due to the condition of electroneutrality, the surface charge s must be balanced by an equal amount of counterions[i]. Writing this out in terms of ρ and using Poisson's equation gives

$$s = -\int_0^{D/2} e\rho dx = \epsilon_0 \epsilon_r \int_0^{D/2} \frac{d^2\psi}{dx^2} dx = \epsilon_0 \epsilon_r \frac{d\psi}{dx}\Big|_{D/2} - 0 = -\epsilon_0 \epsilon_r E_{D/2}\,, \tag{2.20}$$

where the penultimate step follows from the field at the midpoint between two like-charged plates being zero. Plugging this result into Equation 2.19 leads us to the expression

$$\rho_{D/2} = \rho_0 + \frac{s^2}{2\epsilon_0 \epsilon_r k_B T}\,. \tag{2.21}$$

From this we see that, even for isolated plates, the number density of counterions has a positive value which goes with the square of the charge density of the surface.

2.1.3.c Putting It All Together: DLVO Theory

Attempting to describe the interaction of charged surfaces with Van der Waals attraction between them leads us to Derjaguin-Landau-Verwey-Overbeek theory. As depicted in Figure 2.3, we see that the net effect depends strongly and characteristically on the surface charge density. While the Van der Waals attraction exceeds the surface repulsion at low distances, the two surfaces must first overcome an energy barrier that may be prohibitively high. For weakly charged surfaces, the curve approaches that of pure attraction. In intermediate cases, there may also be a secondary minimum, which would result in a stable dispersion. Though not depicted in the image, the existence and extent of these features is additionally affected by the choice of electrolyte. This is a

[i] We consider the surface charge given in units of Cm^{-2}, also known as charge per surface. This means that the number density of counterions over the available area still needs to be scaled by the charges of the counterions.

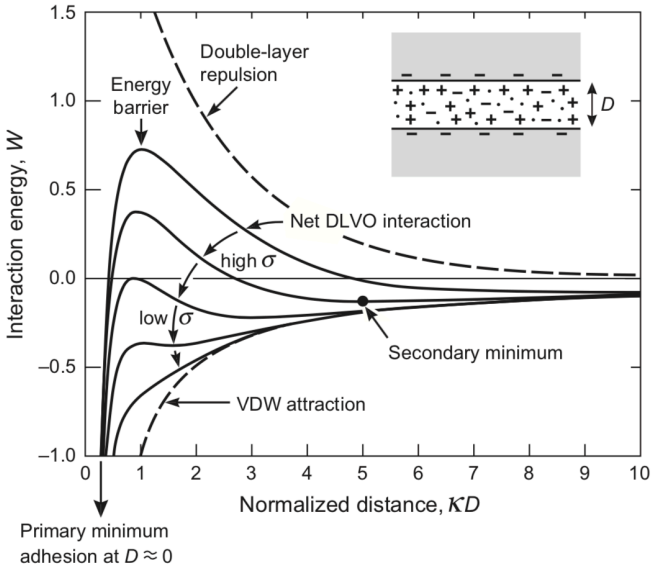

Figure 2.3: DLVO interaction energy of two surfaces at distance D for different surface charge densities σ, with the distance normalized by the inverse Debye length κ to account for screening. This image is from[13]

consequence of the screening discussed in the previous section, which can significantly dampen the electrostatic repulsion.

Like in Section 2.1.2.a, we can attempt to find the total DLVO interaction energy of two colloids considering their geometries. The derivation is more complex and would require the introduction of several concepts otherwise not relevant to this thesis, so we simply present the results for the geometries of two flat planes (Df) and two spheres of radius a (Ds):[13]

$$U_{Df}(r) = -\frac{\kappa}{2\pi} Z \exp(-\kappa r)\,, \tag{2.22}$$

$$U_{Ds}(r) = -\frac{a}{2} Z \exp(-\kappa r)\,. \tag{2.23}$$

Here the interaction constant Z serves a similar purpose to the Hamaker constant A in characterizing the strength of the interaction without considering the influence of the geometry, solution and distance. It is given by

$$Z = 64\pi\epsilon_0\epsilon_r \left(\frac{k_B T}{e}\right)^2 \tanh^2\left(\frac{e\psi_0}{4k_B T}\right)\,. \tag{2.24}$$

Through years of experimental study, DLVO theory has been shown to be sound in typical settings[13]. Deviations tend to occur either when additional forces are at work, or at small distances, due to the influence of the Stern layer and the finite size of the (counter-)ions.

2.1.4 Brownian Motion

Unlike the forces considered in the previous subsection, Brownian motion is a stochastic effect. It arises from thermal fluctuations in the solvent, which perturb the molecules of the solvent. Those particles are constantly colliding with the colloidal particles in suspension. The result is that colloids have an observable "jittering" motion. It also means we can't ignore thermal fluctuations when designing our model. This will motivate us to chose the Langevin equations of motion (see subsection 2.2.2) to describe the movements of the particles, which incorporate Brownian motion by adding a Gaussian random force term.

2.2 Simulation

To paraphrase Frenkel and Smit[20], many basic laws of nature are expressed in equations that have the unpleasant property of not being analytically solvable. This is where computer simulations can come in and deliver a numerical solution of sufficient accuracy. Or they can be used to replicate an experimental system in silico to gain insight into its behavior, and perhaps explain surprising outcomes. A third avenue is to perform "computer experiments" when physical experiments would be costly, dangerous or impossible[21]. This breadth of applications has given rise to a variety of methods. Since a satisfactory answer to the driving question of this thesis ("Why do cubes self-assemble?") needs to explain the motion of the colloids, we will focus on the method which most accurately reproduces the trajectories of the particles, namely Molecular Dynamics simulations.

2.2.1 Molecular Dynamics

Any conventional simulation method for colloidal systems will involve simulation "particles" with certain positions and momenta, alongside interaction potentials which describe the potential energy of the system[20]. A common assumption in this context is that classical mechanics suffices to describe the motion of molecules. This is the outset of Molecular Dynamics methods: given particles and potentials, we use Newton's equations of motion to calculate the time evolution of the system. As the state of our system is determined by particle positions $\mathbf{x}(t)$ and momenta $\mathbf{p}(t) = m\dot{\mathbf{x}}(t)$, this means we need to use

$$\mathbf{F}(\mathbf{x}(t)) = m \cdot \ddot{\mathbf{x}}(t) \tag{2.25}$$

to obtain those quantities. Since we know the potential energy $\mathbf{U}(\mathbf{x}(t))$, we can compute the force $\mathbf{F}(\mathbf{x}(t)) = -\nabla\, \mathbf{U}(\mathbf{x}(t))$. We can also reformulate the equations of motion to be solved as first-order

differential equations[22]:

$$\dot{\mathbf{x}}(t) = \frac{\mathbf{p}(t)}{m} \quad \text{and} \quad \dot{\mathbf{p}}(t) = m \cdot \ddot{\mathbf{x}}(t) = \mathbf{F}(\mathbf{x}(t)) \ . \tag{2.26}$$

These can be solved numerically, but require initial conditions. Since we do not know all the positions and momenta of all the particles in the system at time, we introduce a warm-up phase into the simulation that can move the particles into physically meaningful configurations. During the warm-up, the system is integrated from the starting configuration until it reaches equilibrium. From this point on, the observable properties of the system can be sampled. After a sufficiently long sampling time, we compute our desired quantities by averaging over those measurements. These are time averages, not the ensemble averages from statistical physics on which our analysis of the system is based. That we may treat these two as interchangeable is an assumption known as the ergodicity hypothesis: specifically, we assume that any average of a function of the coordinates and momenta of a many-particle system can be computed either by time averaging or by ensemble averaging[20]. These ideas can be distilled into a workable approach by the following the structure outlined in Algorithm 1:

Algorithm 1: Molecular Dynamics

```
1  read input parameters;
2  initialize particle positions and velocities;
   /* Warm up                                          */
3  for t= 0 to t_eq do
4  |  compute forces;
5  |  integrate;
6  end
   /* Main MD Loop                                     */
7  for t= t_eq to t_N do
8  |  compute forces;
9  |  integrate;
10 |  sample;
11 end
```

While it may seem obvious to start with the reading of input parameters, we highlight it here for two reasons. First, it enables the reuse of scripts by varying parameters. This should be considered when structuring the code. Second, the input to be read in is not limited to a few values- it is possible to load in all the information defining a simulation system of interest at any point in time. As the standard practice is to initialize particle positions on a lattice or place them randomly[20], neither of which are equilibrium configurations for our system of interest, an informed choice of initial particle positions can dramatically reduce the time needed to equilibrate the system.

The first few integrations of the warm up serve to resolve overlaps that can occur when particles

are placed randomly. This can be considered a technical issue, as the steric repulsion of overlapping particles can give rise to a force large enough to crash the simulation. During this phase, one can set an artificial upper limit on the forces applied to particles (a cap) to make the simulation stable. The rest of the warm up serves to equilibrate the system. We presume that equilibrium is reached once the properties of the system reach a constant value but for thermal noise[20]. This means we do not know the time to equilibration t_{eq} a priori. Instead, we run trials of the simulation and monitor the values of the quantities of interest (e.g. the energy), then choose a safe number of timesteps after which the sampling can begin.

Both the warm up and the main loop contain two lines which form the core of this method: computing the forces and integrating the equations of motion. Calculating the force also forms the most computationally expensive part of such simulations[20,21]. This is not due to the expression-evaluating the negative gradient of the potential energy is straightforward - but because the number of pairwise interactions in a system of N particles grows with N^2. The key making this manageable is to speed up the (implicit) first step of checking if particles are within cutoff distance of each-other (see Section 2.2.3.a). Despite such measures, this scaling places an upper bound on the amount of particles we can simulate in a reasonable time.

Once the forces are known, the actual integration of the equations of motion is handled by a subalgorithm often referred to as the integrator[22]. The standard choice of subroutine is some finite difference scheme derived from a Taylor expansion of the particle coordinates, such as the Verlet Algorithm, the Leapfrog Algorithm or the Velocity-Verlet Algorithm[21]. When selecting a molecular dynamics integration algorithm, the focus is on its accuracy in reproducing trajectories and its upholding of physical laws like microscopic time reversibility and the conservation of momentum and energy. Since the computation time is dominated by the force contribution, the speed of the algorithm is not optimized directly. Instead we seek an algorithm that is accurate and stable enough to admit a large timestep, which reduces the number of times forces need to be computed. Other traditional requirements include economical use of memory and ease of implementation[21], which have decreased in importance due to advances in computing hardware[20] and the nascence of MD-specific software packages.

After sufficiently many integrations for the system to be considered to be at equilibrium, measurements of any system properties which can be expressed in terms of particle positions, velocities or momenta can be sampled and averaged over multiple configurations. Here, care should be taken to choose a large enough sampling interval to avoid spurious correlations. It may also be useful to write out the trajectories in a visualization-compatible format and to checkpoint the system periodically. The extent to which raw values are written out for offline analysis versus properties being computed in the simulation will depend on the runtime and computational cost. Some visualization of the results will need to take place in any case.

The results we obtain are to be interpreted and analyzed as ensemble averages based on the

framework of statistical physics. Although these values are independent of the ensemble chosen in the thermodynamical limit, the simulation process itself is not. Classical Molecular Dynamics simulations as described in Algorithm 1 are performed in the microcanonical (NVE, with V as volume and E as energy) ensemble[21]. Depending on which properties of the system are under investigation, other ensembles may be more suitable.

2.2.2 Langevin Dynamics

As this thesis describes an experimental system with unknown energy at a constant (known) temperature, we choose the canonical (NVT, where T is the temperature) ensemble for our simulations. This will require some modifications to our current scheme, which offers no possibility to control the temperature. Our method also lacks a representation of Brownian motion. Both of these issues can be resolved by using the stochastic Langevin thermostat algorithm.

In thermodynamics, a system can be kept at constant temperature by coupling it to a heat bath. To implement a thermostat, we will translate this concept into simulation. One way to go about this is to modify the equations of motion, so that each simulation particle is subject to a random force $\mathbf{X}_T(t)$ and torque $\mathbf{X}_R(t)$ representing the influence of the heat bath. This can be described by using the Langevin equation of motion[23]:

$$m\,\ddot{\mathbf{x}}(t) = \mathbf{F}(\mathbf{x}(t)) - \gamma_T\,\dot{\mathbf{x}}(t) + \mathbf{X}_T(t)\,, \tag{2.27}$$

with friction coefficient γ_T to characterize the dynamics of the system. Since our colloidal particles do not have rotational symmetry, we are also interested in the change of their angular velocity ω(t):

$$\mathbf{I}\cdot\dot{\boldsymbol{\omega}}(t) = \boldsymbol{\tau}(t) - \gamma_R\,\boldsymbol{\omega}(t) + \mathbf{X}_R(t)\,, \tag{2.28}$$

where $\mathbf{I}$ is the inertia tensor, $\boldsymbol{\tau}$ is the torque acting on the particle, γ_R is the rotational friction coefficient and $\mathbf{X}_R(t)$ is the random torque[22]. To ensure these random forces and torques accurately represent the fluctuations they model, they follow a Gaussian distribution with a mean of zero and a variance given by the fluctuation dissipation theorem[24]. Introducing the superscripts i and j different particles, and the notation $\delta_{\dots}$ for the Kronecker and $\delta(\dots)$ for the Dirac delta function, the fluctuation dissipation theorem for the random force reads[25]:

$$\langle \mathbf{X}_T^i(t)\cdot\mathbf{X}_T^j(t)\rangle \;= \delta_{ij}\delta(t-t')\,6\,k_B T\,\gamma_T\,. \tag{2.29}$$

The same relation holds for the random torque, albeit with the torque friction coefficient γ_R.

2.2.3 Implementation

Simulations were performed using the Molecular Dynamics software package ESPResSo-3.3.1[26]. Among other features, it provides an implementation of the Velocity-Verlet alogrithm, a Langevin thermostat for NVT ensembles, and supports all the potentials described in previous subsections. For data analysis and processing, a combination of ESPResSo provided routines, Mathematica, tcl, python and bash scripts were used, along with gnuplot, matplotlib and vmd to plot and visualize the results. The software ColorBrewer v2.0 was used to assist in putting together color blind safe palettes.

2.2.3.a Reducing Computational Cost

Several different approaches were used to render the simulations computationally tractable. Firstly, ESPReSo already uses two methods called cell lists and Verlet lists, which keep track of particles within cutoff distance of each-other to save time on force computation. As the simulations in this thesis had to be run with non-periodic boundary conditions to prevent mirror images from falsifying the potential measurements, and with small box sizes to maintain realistic chemical potential near the colloids, parallelization was limited to running scripts with different parameters simultaneously. The hardware for this was provided by the Vienna Scientific Cluster VSC-3. Another method utilized to lessen the computational cost was checkpointing. This reduced the time necessary for equilibration, as simulations could be (re-)started from preprocessed configurations with realistic particle distributions. The checkpoints also enabled off-line analysis of the resulting configurations.

2.2.3.b Creating Cubes from Spheres

The work presented this thesis rests on the superball model developped by Donaldson et al.[27], who were kind enough to provide the actual code of the `tcl` implementation. Given a choice of shape parameter q derived from experimental observations (see Appendix 7.1), this model approximates the shape of a superball using a set of spheres fitted to the curvatures of the vertices and edges[22], as illustrated in Figure 2.4. An additional sphere is placed in the center of the arrangement to provide the surface of the faces and to position the center of mass. This allows us to use ESPResSo's `Virtual Sites` feature: each of the spherical particles may interact with its environment, functioning as the surface of the cubes, but the equations of motion are only integrated for the central particle. The other spheres, the "virtual particles", are attached to the central "real" sphere at a fixed distance and derive their positions and velocities from it. When these spheres experience forces or torques, these are passed to the central particle. As a result, we are able to approximate a much more complex particle geometry at low additional cost.

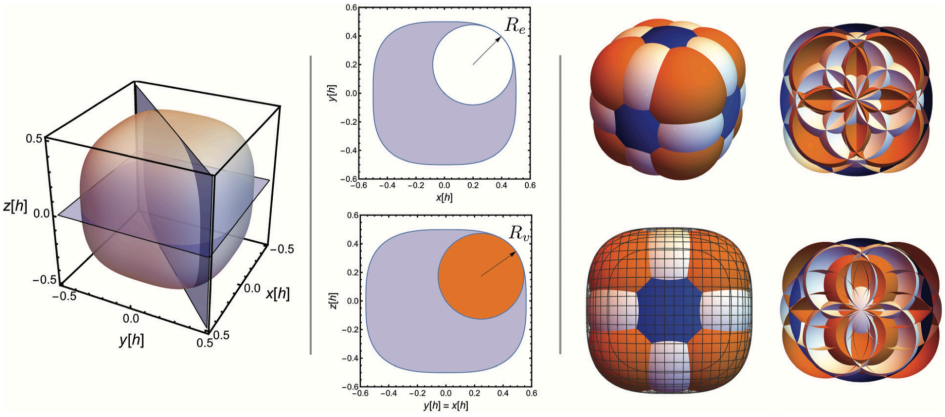

Figure 2.4: Excerpted from[27], we see the analytical shape of the superball (left), a depiction of how spheres representing edges and vertices are fitted to the superball surface (center) and the full model for use in simulation (right), each for a shape parameter of $q = 1.5$.

2.2.4 Miscellaneous Considerations

As this section concludes, the reader may still miss certain forces and considerations. We omit gravity as its effects would not be significant in the short timescales under consideration. Hydrodynamics and friction would have been an interesting addition, but are not computationally feasible within the chosen framework. While this chapter is by no means comprehensive, we posit that it contains the necessary elements to construct a simple model of colloidal behavior. The aim of this project is not to create a perfect replica of the experimental system: rather, we seek a parsimonious explanation for the effects observed.

3 | The System in silico

To create a model that represents the experimental system, we combine the theoretical knowledge discussed in the previous section with measurements performed by partners at the Van't Hoff Laboratory for Physical and Colloid Chemistry and parameters found in literature. The aim is to find a middle ground between matching experimental values and the computational simplifications necessary to perform any calculations.

3.1 Scaling

To quantify and apply the theory discussed above, we must choose a system of units that scales the experimental system to be computationally tractable. Given our chosen paradigm of energies and equations of motion, there are only three independent quantities to scale: length, time, and mass. As accurate energies are key to achieving aim of this work, we define our scales for length, energy and mass, as these four quantities are related via $[\text{energy}] = [\text{mass}] \cdot [\text{length}]^2 \cdot [\text{time}]^{-2}$. Although the standard approach to reducing units involves dividing by the characteristic parameters of the scale in question[20], we will sometimes sacrifice this convention for the sake of easier tuning and comparison of parameters. For this reason, the standard notation of (*) for reduced units is not used. However, some rescaling of the experimental parameters remains necessary to avoid numerical issues (underflow, loss of precision) with handling numbers very much smaller than one.

3.1.1 Length Scale

The choice of length scale was predicated by two experimental observations: the height of the cubes (90 nm) and number density of the negative surface charges ($5 \cdot 10^{-3}$ to $10 \cdot 10^{-3}$ per nm^2). A length scale with small cubes is computationally cheaper: it requires fewer surface charges and counterions, and has shorter interaction ranges, which would allow us to shrink the simulation box. However, the explicit surface charges require explicit counterions to maintain charge parity, which must have a minimum "size" for computational stability. This size should still be significantly smaller than the colloids. The low charge density also imposes a bound on the length scale in that the fewer charges are present, the more the distribution of the charges will influence the resulting interactions.

Taking these considerations into account, the length scale was chosen to correspond exactly to nm. This means that one simulation cube has the diameter $\sigma_c = 90$nm. The diameter of counterions and surface charges was set to 1 for simplicity and computational stability. Lesser ion diameters would result in steeper steric repulsion, which resulted in a less stable system in the

tests run. If we estimate the surface of the cubes to be approximately $A = 6 \cdot 90^2 = 4.86 \cdot 10^4$ nm^2, using the higher estimate for the density of surface charges to see the greatest possible influence of the shape and the electrostatic system aspects, this gives approximately $4.86 \cdot 10^{4-2} = 486$ charges per cube, or 81 charges per cube face.

One drawback of this scaling is that the box sizes become inconveniently large in simulation units. This can be mitigated by listing the box lengths in units of cube length σ.

3.1.1.a Adaption of the Colloid Model

As a first corollary of our scaling, we rescale the cube model to σ_c and extend it by adding virtual point charges to the analytical superball surface $\mathscr{S}$. The initial model was developed for a cube with shape parameter $q = 2.0$, then adapted to $q = 1.7$ to better approximate the curvature seen in experiment (see Appendix 7.1). As seen in Figure 3.1, these changes required the inclusion of additional spheres to better approximate the edges[22]. To ensure that the symmetries found in cubes were retained, the charges were distributed almost uniformly by placing the amount of charges per face $-$ 81 $-$ on a 2D grid, then computing the third coordinate of the charge position via the analytical superball equation. This requires the definition of "edges", characterized by the value e_b which is the largest value for which a z exists such that $(e_b, e_b, z) \in \mathscr{S}$, and corners, which are defined by $(c, c, c) \in \mathscr{S}$ such that $\sqrt{3c^2}$ is maximal. Each "face" runs from edge to edge, with an adjustable edge border ensuring that charges from different faces are not placed in excessive proximity. Corners must treated separately, as each of the six grids would place four charges on corners of the cube, resulting in three charges per corner. These are removed and replaced by a single charge per corner, reducing the total number of charges to $N_c = 486 - (3-1) \cdot 8 = 470$. Placing the charges on the analytical surface also leads to their centers protruding slightly above the cube-composing spheres in many areas. This is intentional, to allow counterions to settle on the surface without being pushed away during assembly.

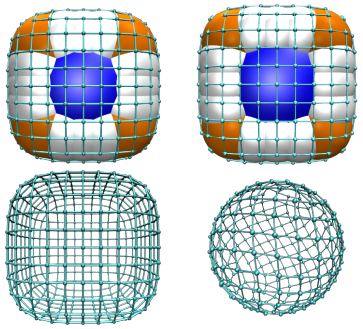

Figure 3.1: Top: simulation model for $q = 1.7$ (left) and $q = 2.0$ (right); images below show the grid of counterions for $q = 1.7$ and $q = 1$.

3.1.1.b Charged Spheres

To be able to distinguish the influence of the anisometry from other forces at play in the system, we create a reference model of charged spheres. The number of charges on a sphere with a diameter of 90nm, given the same charge density as the cubes, is $(4\pi \cdot 45^2) \cdot 10^{-2} \approx 254$. However, distributing n points on uniformly on a sphere is a nontrivial mathematical question. We chose the Fibonacci lattice approach, which has been shown to yield a more spatially homogenous distribution

of points than traditional lattitude/longitude lattices[28]. In this method, the distribution of points is given by a Fermat spiral with a longitudinal angle of the golden ration Φ between consecutive points.

To implement this idea in simulation, we generate a sequence of points in spherical coordinates (r, θ, ϕ). The jth point will have an r coordinate of 45, as this is the radius of the sphere, and an azimuthal angle of $\phi = j \cdot \Phi$ due to the Fibonacci condition. The polar angle θ is given by

$$\theta = \arcsin\left(\sqrt{1-z^2}\right) \quad \text{, where} \quad z = \left(1 - \frac{1}{N_c}\right) \cdot \left(1 - \frac{2j}{N_c - 1}\right) \quad . \tag{3.1}$$

To be mathematically rigorous, the spatial homogeneity of the distribution holds only for an odd number of points N_c. This isn't an issue for our model, since we do not expect equidistribution of charges in the experimental system and thus did not enforce it in the distribution of charges on the superball. The goal here is to distribute the charges uniformly enough that there is no rotational anisometry in our model of fully rotationally symmetric colloids.

3.1.1.c Characteristic Length Scales of the Electrostatic Interactions

Given a temperature of $T = 293\text{K}$, we compute the Bjerrum length using Equation 2.10 and the Debye length using Equation 2.12:

$$l_B = \frac{e^2}{4\pi\epsilon_0\epsilon_r k_B T} \approx \frac{57.03}{\epsilon_r}\ \text{nm} \quad \text{and} \quad \kappa^{-1} = \sqrt{\frac{1}{8\pi\, l_B N_A I}} \approx 0.034 \cdot \sqrt{\frac{\epsilon_r}{I}}\ \text{nm}\ .$$

The dielectric constants of common solvents have been thoroughly investigated, and thus accurate values are readily available in literature[29]. To emulate the experimental system, we require models for water and ethanol:

Solvent	Dielectric const. ϵ_r[29]	Bjerrum length l_B
Water	80	0.71 nm
Ethanol	25	2.28 nm

Table 3.1: Computed Bjerrum lengths for the simulated solvents

To approximate the screening effects in a salty solution, we need to calculate the ionic concentration. Based on the experimental parameters obtained from our collaboration partners (see Appendix 7.1), we only consider a monovalent salt (e.g. sodium chloride) dissolved in pure water. This means that the charge numbers z_i of the ions are ± 1, and that the molar concentrations c_i are equal. This allows us to simplify Equation 2.11 to obtain

$$I = \frac{1}{2}\sum c_i z_i^2 = \frac{1}{2}\left(c\cdot(-1)^2 + c\cdot 1^2\right) = c \ .$$

In other words, the ionic concentration reduces to the molar concentration of the salt. For our range of concentrations, this gives:

Ionic concentration I	Debye length κ^{-1}
10^{-3} molar	9.63 nm
10^{-4} molar	30.44 nm
10^{-5} molar	96.27 nm
10^{-6} molar	304.43 nm
10^{-7} molar	962.71 nm

Table 3.2: Debye lengths for each of the ionic concentrations simulated.

3.1.2 Mass and Time Scale

In principle, the mass m of our colloids is known, or at least easy to estimate. A hollow superball of shape parameter $q = 1.7$, height $\sigma_c = 90$ and thickness of approximately 10nm has a volume of[22]:

$$V(1.7,90) - V(1.7,80) = \frac{\Gamma\left(\frac{1}{2\cdot(1.7)}\right)^3 (90)^3}{12q^2\Gamma\left(\frac{3}{2\cdot(1.7)}\right)} - \frac{\Gamma\left(\frac{1}{2\cdot(1.7)}\right)^3 (80)^3}{12q^2\Gamma\left(\frac{3}{2\cdot(1.7)}\right)} \approx 658441 \text{ nm}^3. \tag{3.2}$$

The density of silica is $1.5-1.8$g per mL (see Appendix 7.1), which gives us:

$$m = 1.5\cdot 10^{-21}\cdot 658441 \approx 9.9\cdot 10^{-16} g. \tag{3.3}$$

In comparison, the mass of a hydrogen ion is roughly $1u \approx 1.7\cdot 10^{-24} g$. Such a gap of 9 orders of magnitude cannot be translated directly into simulation. Seen as a timescale question, we must find a way to accommodate both the rapid motion of counterions and the slower agglomeration of the cubes, which took 8 to 14 days to fully equilibrate in initial experiments[3].

This is slightly mitigated by our omission of hydrodynamics, which accelerates the assembly process and is vastly cheaper in computational terms. However, this also raises a host of new problems. More specifically, in a naive model, the simulation cubes will rotate just as a sphere would, since the virtual particles forming edges and corners have no mass, and experience no form of inertia, friction or drag.

This means that, aside from setting a centralized mass to control the translational diffusion of the colloids, we must also imbue them with a rotational inertia to make their rotational diffusion

realistic. ESPResSo supports this, allowing the user to set the moments of inertia with respect to the particles' coordinate axes. For a hollow cube, these are given by $I = \frac{5}{3}mh^2$, where h is the height of the cube[30]. This relation between rotational and translational inertia will need to be conserved.

Finally, to obtain parameters that could be used in simulation, we began with choosing a small but acceptable timestep $t = 0.005$ for the simulation and the smallest computationally stable mass for counterions, $m_{ci} = 1$. Then, we tested pairs of parameters (m, I) to find a computationally stable set with values low enough to let the cubes diffuse, and high enough to avoid unphysically fast movements. The smallest stable mass found was $m = 50$, which corresponds to a moment of rotational inertia of $I = 675000$.

Quantitatively, these values clearly don't correspond to any experimental parameters. However, we will see that the results qualitatively describe the dynamics of the system in a way that, based on established physical theory, can explain the behavior seen in experiment.

During the tuning process, we also attempted the alternative approach of modifying the Langevin friction coefficient γ to gain control over the diffusion. This is theoretically sound, but the method as currently implemented in ESPResSo could only operate on the central sphere, which failed to resolve the rotational diffusion issues.

3.1.3 Energy Scale

The key to understanding the dynamics of the cubes lies in accurately representing the balance of the forces acting on them. As the electrostatic interactions have already been set, based on experimental parameters and length scaling, only the Brownian motion (thermal fluctuations) and the Van der Waals forces remain. Since we know the temperature of our system, the thermal energy is given by $k_b T = 293 \cdot 1.38065 \cdot 10^{-23}$ J ≈ 4 zJ[i]. This quantity already parametrizes our thermostat. For it to produce thermal fluctuations strong enough to affect the system, but not so strong as to require the use of an exceedingly small timestep, it should be scaled to lie in the order of magnitude of 1.

This is usually done by giving the energy of units in $k_B T$, i.e. setting the scaling so that the thermal energy is one. The main arguments for this scaling is to avoid potential redundancies (rerunning equivalent simulations) and simplicity[20]. However, in this case the former does not apply, since finding a single set of functional simulation parameters took months of testing and tuning. As Hamaker constants are commonly given in zJ, including additional factors to the scaling seemed to increase the complication of fitting to experimental parameters. For these reasons, the energy scale was set to zJ, with $k_B T = 4$. Setting the energy scale parameter of the Lennard-Jones potential also defines the scaling of the steric repulsion, so we will only need to consider the

[i] Here zJ stands for zeptojoule: 1 zJ $= 10^{-21}$J.

attraction strength to obtain the remaining interaction parameters.

3.1.3.a Strength of Van der Waals Attraction

Combining Equations 2.3 and 2.7, we obtain $A = \pi^2\rho^2 \cdot 4\epsilon\sigma^6$ for the relation of the Hamaker constant A to the Lennard-Jones energy parameter ϵ. Unfortunately, we cannot just insert experimental data and obtain a suitable value of ϵ. Firstly, we do not know the Hamaker constant of the cube-cube interaction: we can only make educated guesses based on the constants of similar materials reported in literature. Secondly, our model's decoupling of the simulation mass from experimental measurements isn't considered in the equation above (ρ is the number density). It's also worth noting that the Hamaker constant does not contain any information about the geometry or size of the interacting bodies, since as far as the theory is concerned, this should be considered in the expression for the potential. For completeness sake, we can use the Hamaker constant $A_{SWS} \approx 10$zJ of SiO_2 interacting with SiO_2 across water[18] to compute $\epsilon \approx 5 \cdot 10^{-13}\rho^{-2}$. The result depends on how the density is rescaled.

Moreover, previous work has found indications that the theoretical values underpredict the interaction strength to an extent that it can not explain the behavior observed in experiment[3]. This issue is exacerbated by our model of the cube as the superposition of overlapping sphere surfaces to capture the "bumpiness" of the surface, and our use of the Lennard Jones potential, which results in an attraction that does not match the analytical expression of the Van der Waals attraction between cubes (see Equation 2.4). Notwithstanding this, moving from a centralized, rotationally symmetric potential to a more diffuse attraction is an essential step in obtaining a more realistic model.

Moving forward, we rely on two experimental observations to guide us: firstly, that the Van der Waals attraction is strong enough for the cubes to self-assemble in water[3], and secondly, that it is not strong enough for cubes to self-assemble in ethanol[1]. Using Equation 2.6, we can calculate that the Hamaker constant of silica in ethanol, given $A_E = 42$ zJ and $A_S = 65$ zJ[13,18], is $A_{ESE} \approx \left(\sqrt{65} - \sqrt{42}\right)^2 \approx 2.5$ zJ.

This constrains our range of potential ϵ values, since whatever multiplicative scaling factor is used on the Hamaker constant must result in assembly for $A = 10$ and colloidal stability for $A = 2.5$. Based on test simulations of the system, we can expect the simulation cubes to self-assemble for ϵ values of 10 k_BT or greater. This gives us a range of acceptable values for ϵ, specifically between $10k_B\ T$ and 40 k_BT in water. Since there was no clear choice of "exact value" for this parameter, simulations were run at the lowest acceptable attraction strengths of $10k_BT$ (water) and $2.5k_BT$ (ethanol) to avoid artificially overpowering the electrostatic effects.

3.1.4 Other Considerations - Charge Densities

To maintain an NPT ensemble in a finite box, particles must be prevented from diffusing past its boundaries. This is ensured by adding walls with a hard-sphere steric repulsion. From a physical perspective, we are setting the charge density of the counter-ions in the system by defining how far away from the cube they can distance themselves. This is computationally straightforward, but physically nontrivial since we do not know the charge density in experiment.

To avoid the potential pitfall of influencing the system's electrostatic properties by enforcing an unrealistically high or low charge density, we vary the number charge density $\rho = N_c \cdot V^{-1}$ (where N_c is the number of charges) by varying the box length l:

Box length l	3 σ	4 σ	5 σ	6 σ
Charge Density ρ	$2.39 \cdot 10^{-5}$	$1.01 \cdot 10^{-5}$	$5.2 \cdot 10^{-6}$	$3.0 \cdot 10^{-6}$

Table 3.3: Number charge densities for a single-cube system of varying box lengths.

These values computed for the cube with $N_c = 470$ are shown to illustrate our methodology. Systems with spheres and/or multiple colloids raise the question of whether it is worthwhile to attempt to maintain a specific charge density. This carries the expense of manipulating the box sizes in unconventional ways, which can raise issues with the truncation of interaction ranges and the computational stability in smaller boxes. We also note that these number charge densities do not exclude the volume occupied by the particles. Motivations aside, the issue of charge densities cannot be resolved until we determine if it qualitatively affect the system, which will be discussed in Section 4.2.

3.2 Conclusions

Based on experimental observations and the theory outlined in the previous section, we were able to generalize the existing model of cubical colloids to include electrostatic and Van der Waals effects. These were designed to match experiment as closely as possible. Although not all parameters could be translated directly into simulation due to the extreme differences in mass and timescales of the particles involved, the approximation is faithful enough that it captures the shape effects, and reproduces the experimental system for a variety of solvents with different electrostatic effects.

4 | Electrostatics of a single cube

We begin our investigation of the system by characterizing the electrostatics of a single cube. More specifically, we show how the electric double layer is influenced by the shape, solvent, salinity and charge density. We conclude by measuring the field strength near the cube, which allows direct comparison to analytic results.

4.1 Methods

This section introduces the basic workflow of the simulation script used to generate the raw data for this section. We also explain the fundamental ideas behind the two different analysis methods to characterize the system: our generalization of (radial) density profiles to characterize the electric double layer, and the test charge method for the field measurements.

4.1.1 Simulation Setup and Workflow

The systems studied in this chapter consist of a single colloidal cube fixed in the center of the simulation box, surrounded by counterions to ensure overall charge neutrality. At initialization, these counterions are randomly distributed. The simulation begins with a capped warm-up to safely distance any charges placed in close proximity, then propagates the system in time.

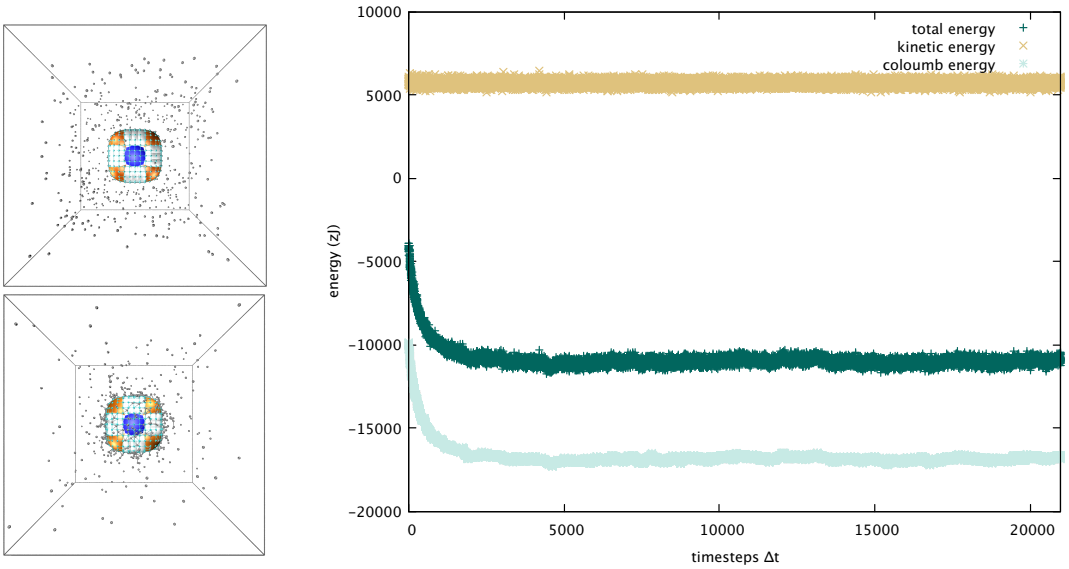

Figure 4.1: Top left: snapshot of the initial configuration of the system. Lower left: the same system at equilibrium, showing the altered distribution of the counterions. Right: plot of the system's energies during equilibration. The system depicted models a cube in ethanol, with the charge density ρ_3 (see Table 4.2).

To determine the amount of integrations needed for the system to reach equilibrium, we monitored the energy in several test runs. One of the plots used to visualize this process is shown in Figure 4.1. As the computational infrastructure at hand made it advantageous to run sets of 16 simulations with different solvent/salinity/density parameters in parallel, we chose the most conservative cutoff of $t = 20000\Delta t$ for all systems. From that point on, the system was sampled at intervals of 100 000 integrations to ensure statistical independence. Each of these samples consisted of a checkpoint and a measurement of the system energy, from which the results were extracted offline.

4.1.2 Density Profiles of Anisometric Colloids

The essence of density profiles as used in this chapter is to characterize the distribution of counterions near a particular geometrical feature of a given colloid at equilibrium. These will provide a stepping stone to characterize the influence of the anisometry of the colloids on their electrostatic properties. The profiles are computed by counting the number of counterions in a given area (bin) at a given distance away from the feature. The raw numbers are then normalized by the volume of the bin for comparison across distances, and the total number of counterions for comparison across shapes. The size of the bins was tuned to find a balance between smoothness of the curves and spatial precision. Overly large bins sacrifice the exact location of the peaks for greater smoothness, and can appear to shift them depending on how the bin length divides the layer. Small bins make the profile appear noisier without contributing additional insight. This tradeoff is depicted in Figure 4.2.

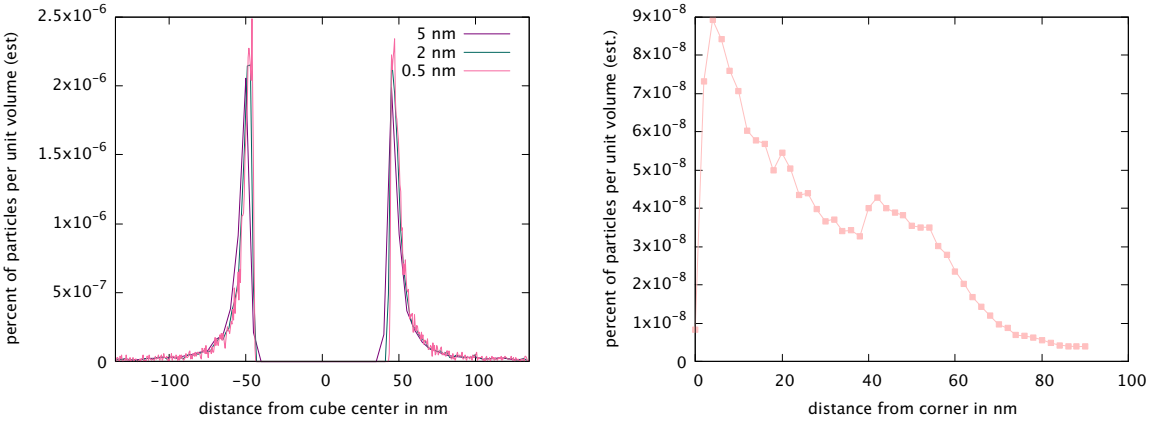

Figure 4.2: The plot on the left shows the effects of varying bins sizes on the appearance of the density profile for a cube face. On the right, we see what a corner based density profile would look like if all of the counterions were included in the evaluation; note the peak at slightly past $40nm$, where the three adjacent corner charges attract counterions.

The next choice to be made is the shape of the bins, which will depend on the shape of the

feature under investigation. This is illustrated in Figure 4.3. In systems containing a sphere, concentric spherical shells were chosen as bins. Differences in normalization aside, this is the same process as computing the radial distribution function for the counterions around the sphere. Moving to cubes, we sought to characterize the distributions of counterions around faces, edges and corners. For the relatively flat surfaces of the faces, we used a series of rectangular bins. The sketch only shows the bins along the x-axis for simplicity, where the distance of the particle from the colloid is taken to mean the projection of the distance onto the x-axis. This was repeated for each set of opposite faces, then averaged. All of these bins are slightly shorter than the faces they are set against, to exclude the counterions attracted to the edges of the cube. This distinction is necessary as superballs have a rounded shape, which means the edges are set slightly farther back than the main face. That positioning introduces a shift in the counterion coordinates, so including these particles in the averaging would artificially smear out the layer.

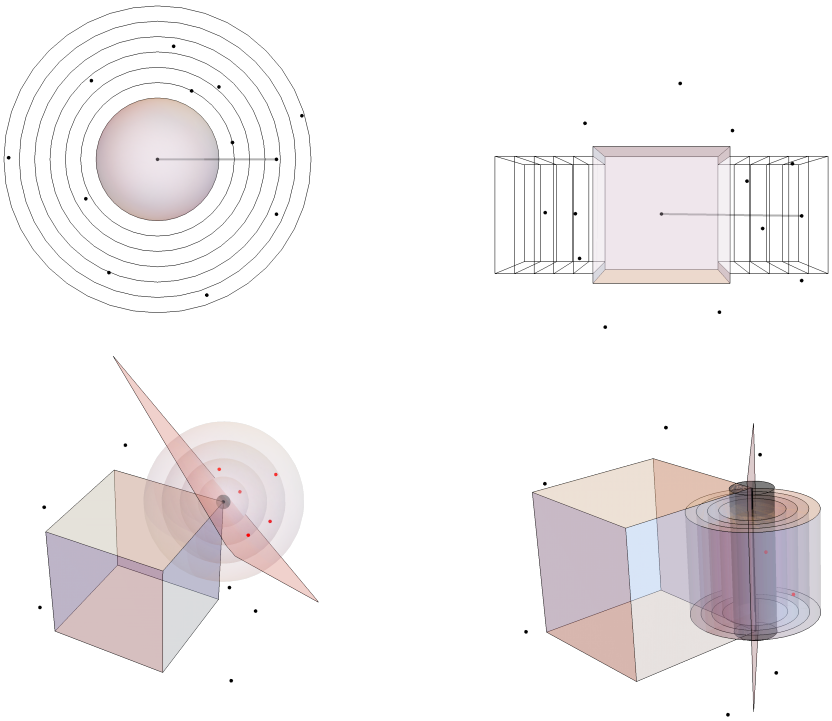

Figure 4.3: Clockwise from top left: cross sections of the binning system for spheres (left) and cube faces (right). All counterion postions in these sketches are for illustrative purposes only and do not reflect a meaningful distribution. The bottom left and right images show the scheme for corner and edge based density profiles respectively. As a visual aid considering the more complex binning criteria in the bottom row, counterions that would be counted in the profile are shown in red.

A similar consideration is made when computing the distribution near a corner. In our simulation model, corners are explicitly represented by spheres, so it seems natural to use a binning

scheme based on radial distance. However, a naive approach would let the profile include counterions attracted to other components of the cube, resulting in an overall boost in density and a secondary peak at the distances of the three nearest corners (see Figure 4.1). To distinguish between the effects caused by different features, we only select the counterions above a plane through the center of the corner sphere, orthogonal to the cube's symmetry axis. This reduces our spherical bins to hemispheres.

Edges combine the challenges of corners and faces. As with faces, there is no clear center from which a radial distance can be defined. This calls for bins extending parallel to the edge, but of shorter height to avoid incorporating the effects of the corners. To exclude the counterions attached to the cube faces, we reuse the plane approach. This time, the plane must pass through the edge and is chosen orthogonal to the symmetry axis through the center of the cube edge. To measure the distances, we chose the in-plane distance between the counterion and the point of the edge at the same height. Combined with the necessity for averaging over the different heights, this gives us concentric cylindrical bins.

4.1.3 Test Charge Method

To measure the electric field strength at any specific point in the system, we implemented a computational version of the test charge definition of the field. A single positive unit charge is placed in at the point of interest $\mathbf{p}$, and, after a brief check for steric overlap, the forces on this charge are evaluated. This is equal to the electric field $\mathbf{E}(\mathbf{p})$. To obtain a description of the whole system, we move our test charge through the system by placing it on each intersection of a 3D grid and evaluating the force there.

While the computational cost of these evaluations is low, frequently interrupting the simulation for these measurements would significantly slow it. This would make the cost of rerunning the field evaluation prohibitively high. Moreover, the amount of evaluations per configuration would scale as l^3 for a box length of l, which then would still need to be averaged over multiple configurations to obtain meaningful results. Therefore, all the results were obtained by reloading saved equilibrium configurations, measuring the field and averaging.

4.2 Results

A total of 32 simulations were run to obtain the data evaluated in this chapter. These consisted of two sets of 16 simulations. One set contained cubes with a shape parameter of $q = 1.7$, and the other was run with spheres. To compare charge densities across these two types of systems with a different total amount of charges, we normalized the number charge densities by the number of total charges in the system.

Symbol	Normalized Charge Density
ρ_3	$5.08 \cdot 10^{-8}$
ρ_4	$2.14 \cdot 10^{-8}$
ρ_5	$1.1 \cdot 10^{-8}$
ρ_6	$6.4 \cdot 10^{-9}$

Table 4.1: Key with notation and values of the different charge densities used.

Both sets of simulations run consisted of eight salt-free runs for the solvent dielectrics of water and of ethanol, with charge densities from ρ_3 to ρ_6. Five of the remaining runs were performed at a density of ρ_3 with the ionic concentration varying from 10^{-3} to 10^{-7} in increments of 10 (see 3.1.1.c). The other three were performed at ρ_6 with the ionic concentrations of 10^{-3}, 10^{-5} and 10^{-7}. This setup deliberately skips some combinations of intermediate parameters, as they are not expected to provide additional insight into the system and would increase the computational cost by at least 50%.

For the field evaluations, we set a plane through the middle of the system and evaluated the field within 50nm of the surface of the colloid, then averaged the values obtained over 10 equilibrated system checkpoints. This range limit was chosen based on the density profiles, which show that the counterion profile reduces to spatial equidistribution past that distance. The amount of checkpoints used was dictated by computational expediency, as these plots are intended to give additional visual and qualitative insight to a system that has already been quantitatively described by the density profiles. In principle, the routine could also be extended to average over a "slice" instead of a plane: however, it is cheaper and simpler to average over multiple checkpoints than over different heights.

4.2.1 Density Profiles

The results in this subsection were extracted from simulation checkpoints as described before, and averaged over 79 configurations. Each set of figures explores a different solvent, with exception of Figure 4.7 which revisits the effects of salinity at a low charge density.

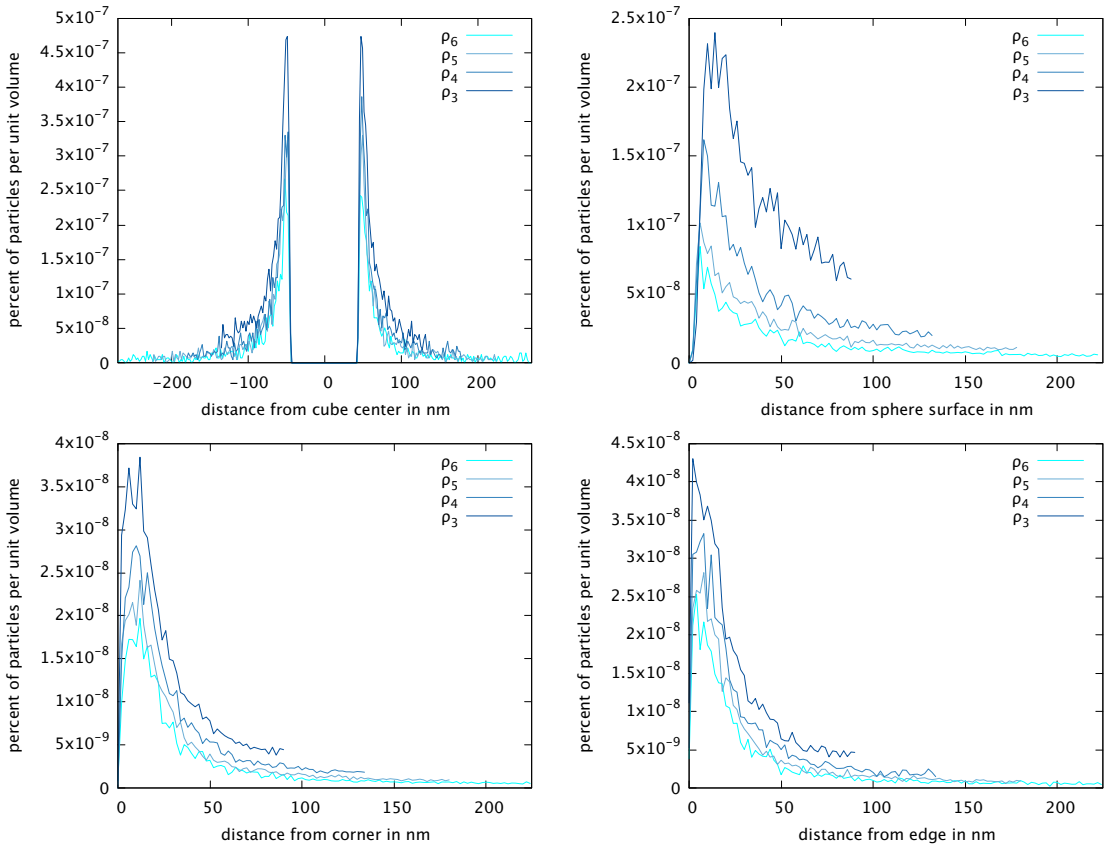

Figure 4.4: Density profile of counterions near the cube in water, with varying charge densities. Going clockwise from the top left, we show the density profile of counterions adjacent to cube faces, spheres, cube edges and cube corners.

In water, shown in Figure 4.4, we see the formation of an electric double layer surrounding the colloid. This supports our amalgamation of implicit and explicit models of different electrostatic system aspects. For each type of profile, we see a characteristic shape that is conserved across different charge densities ρ. It appears steeper in profiles of cubes, most notably that of the cube faces. This shape also varies for different geometric features of the cube in question, showing that the anisometry of the underlying particle gives rise to an asymmetric counterion distribution around it. The profiles of the highest densities appear to be the noisiest, which is plausible given that all counterion in the model are like-charged and therefore repel each-other when close. The slight offset of the peaks in the analysis of sphere profiles may be a result of the differences in modeling, since in that case the surface charges are placed exactly on the steric surface of the particle. For all geometries, the profile collapses into approximate equidistribution (allowing for thermal fluctuations) from roughly $100nm$ past the surface on.

Moving to ethanol as a solvent, depicted in Figure 4.5, we obtain a layer consisting of far more counterions very close to the cubes. Although lower overall charge densities decrease the

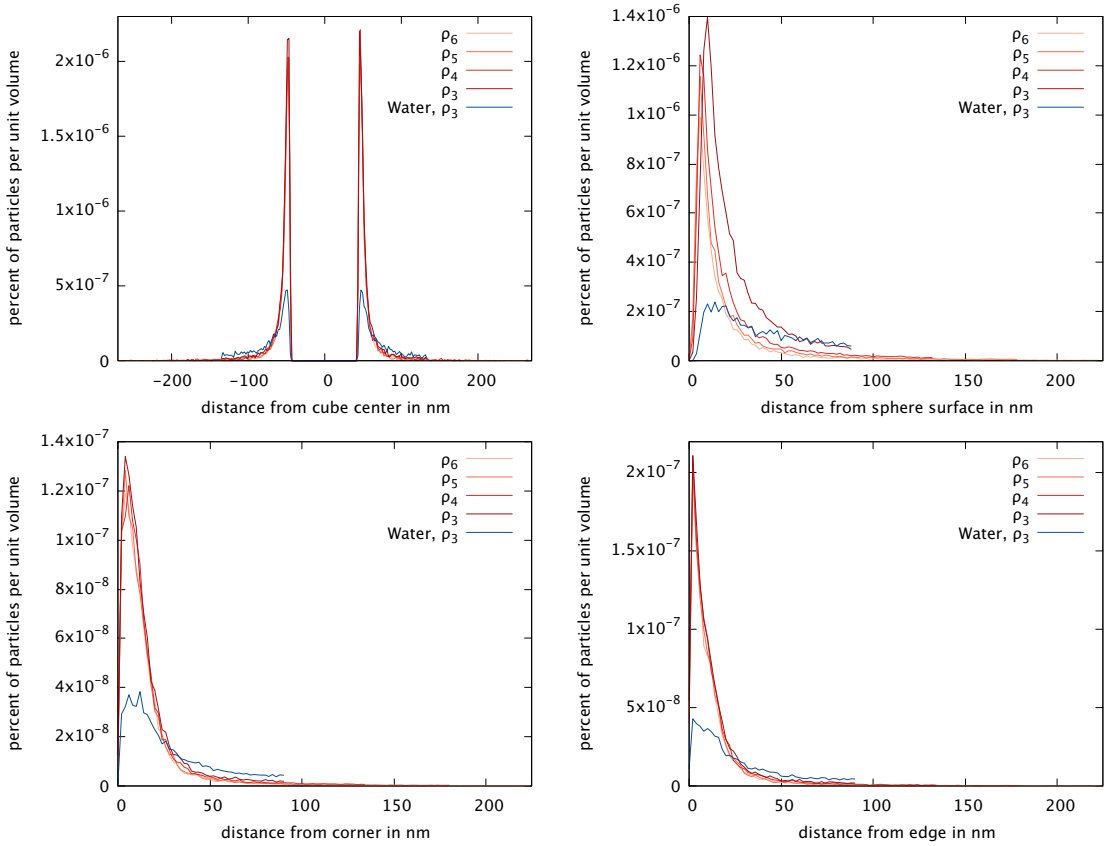

Figure 4.5: Density profiles for varying counterion concentrations in ethanol from cube faces, spheres, cube corners and cube edges. The corresponding counterions distributions in water are included in dark blue for reference.

amount of counterion in the layer, this effect is less pronounced than in water. Noticeably, the peaks for each of the density profiles are more localized and the curves are smoother even across comparable length scales. This is may be caused by the stronger electrostatic repulsion dampening the effects of the Brownian motion of the particles. While the profiles near different features still differ quantitatively, the shapes resemble each-other to the extent that they could be considered identical. While the total number of counterions in the layer has visibly increased, we can note that the proportion of counterions in the layer near different features has been conserved. Interestingly enough, the change in solvent seems to have affected the offset of the layer in the case of spheres, despite all steric properties being identical.

Examining systems with varying salinity at a fixed, high density (Figure 4.6), we first note that in the case of low ionic concentration, the resulting density profile converges to the salt-free case (dark blue line). As the concentration of the salt increases, the layer grows increasingly diffuse and breaks down entirely at sufficiently high salt concentrations. The layer on the cube faces is the most sensitive to the changes in salinity. Although these results are all drawn from the same

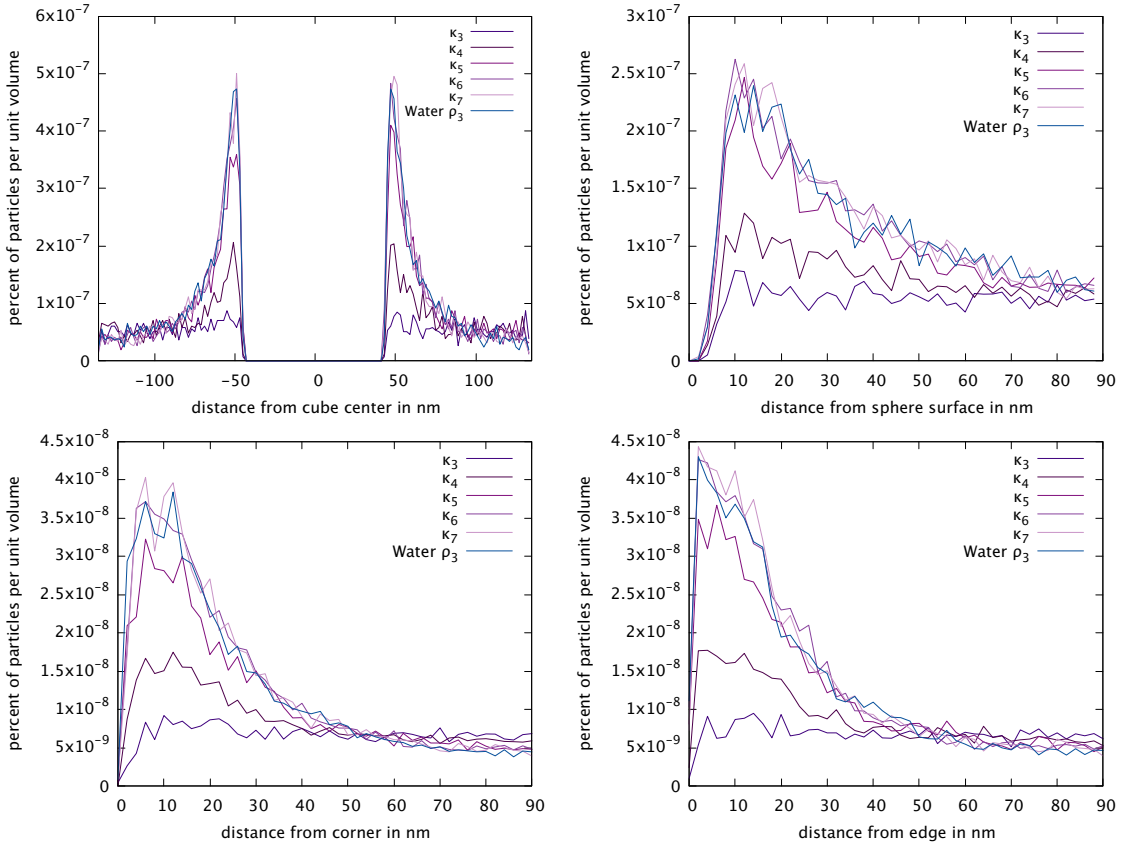

Figure 4.6: Density profile of counterions near the cube in water with varying salinity. Each curve color represents a system at a different ionic concentration, the naming scheme of which follows their order of magnitude, i.e. $I = 10^{-x}$ molar becomes κ_x. The charge density is fixed at ρ_3. As in the previous figure, we show the density profile of counterions adjacent to cube faces, spheres, cube edges and cube corners.

simulations, only the cube faces show non-trivial differences in layer for each salinity value and still attract a layer of counterions for the ionic concentration of $I = 10^{-4}$ molar. For spheres and all rounded features, the ionic concentration either results in layers comparable to those in water for low values of I, or a breakdown of the layer verging on equidistribution at high concentrations. For cube faces and spheres, the counterion density at a distance from the colloid appears to match the "average" normalized charge density for the $I = 10^{-3}$ molar. These results suggest that altering the salinity of the system will result in significantly different electrostatic properties of the colloids. This also determines if the anisometry present in the geometry of the particles is further reflected in the electric double layer.

While the conclusions of the previous figure have practical implications for experiment design, they were obtained using a specific charge density. Although the investigation of the salt-free system in Figure 4.4 showed that altering the charge density does not affect the overall shape of the distribution, this cannot be presumed to hold for all salinities. Choosing the lowest charge

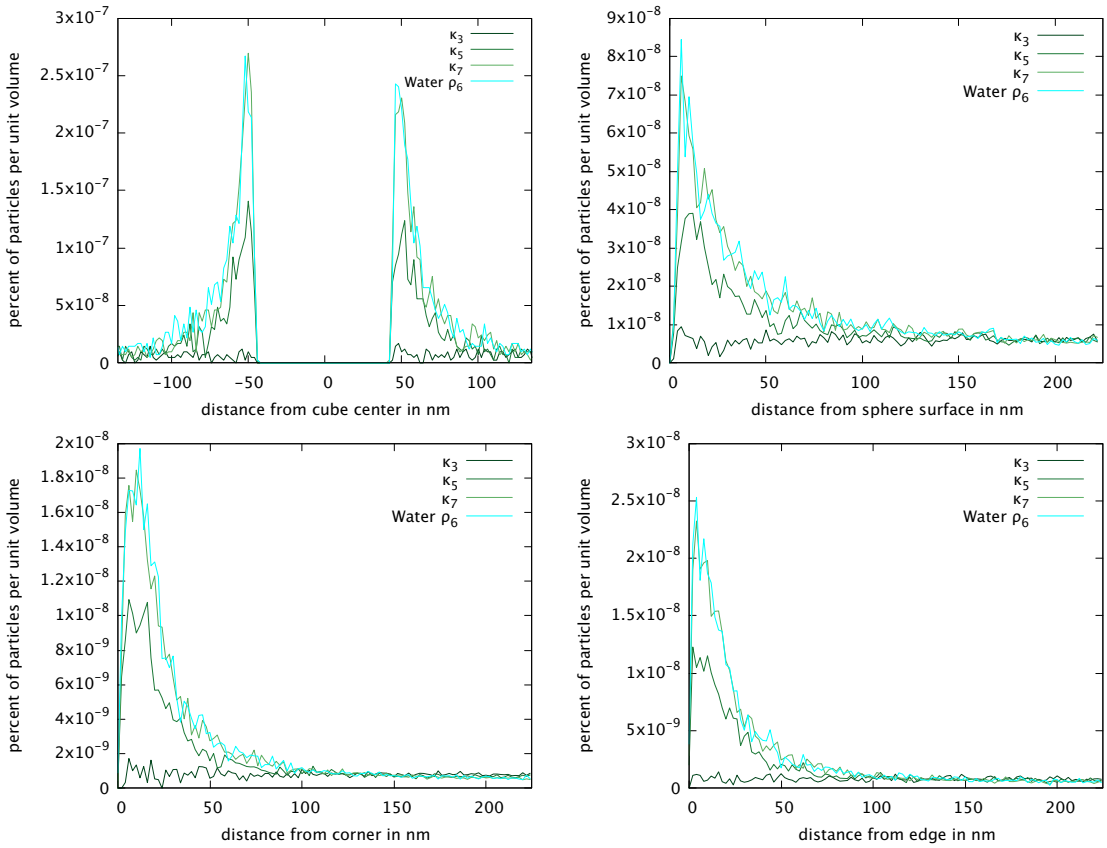

Figure 4.7: Following the naming conventions and layout of the previous figure, we show the density profiles of counterions at the fixed density ρ_6 for three sample salinities.

density, we investigate three sample salinities in Figure 4.7. We find that the breakdown in the double layer begins at a lower salinity than in the previous case. At very high or very low salinity, the profiles are qualitatively similar to those in Figure 4.6, allowing for the expected lower average density and peak height. We also see the same agreement with the salt-free case for low salinity. Whether or not the intermediate stage seen here also occurs in a similar form in high density systems is not clear. It is interesting to note that increasing the salinity of a low density system shows a similar effect as decreasing the density in a salt-free system.

Still, we see that the electric double layer retains its qualitative properties for colloids in water, ethanol and salt water of very high or very low salinity independent of the charge density, and only the intermediate cases need to be treated with caution.

4.2.2 Field Measurements

This subsection explores the electric field strength near a cubical or spherical colloid for the systems discussed in the previous subsection. Figure 4.8 shows that for cubes, the decrease in field

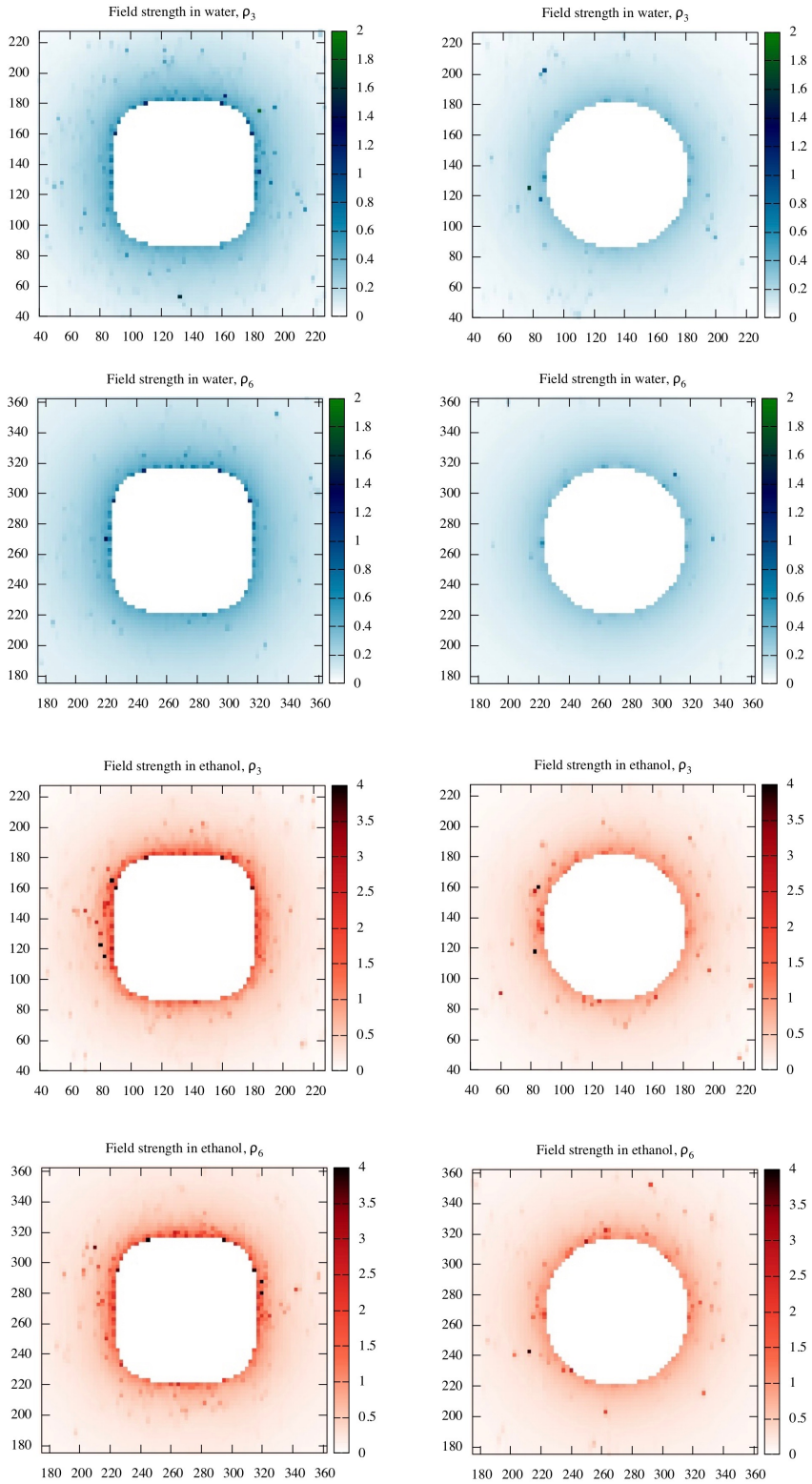

Figure 4.8: The strength of the electric field near cubes (left) and spheres (right) in different solvents.

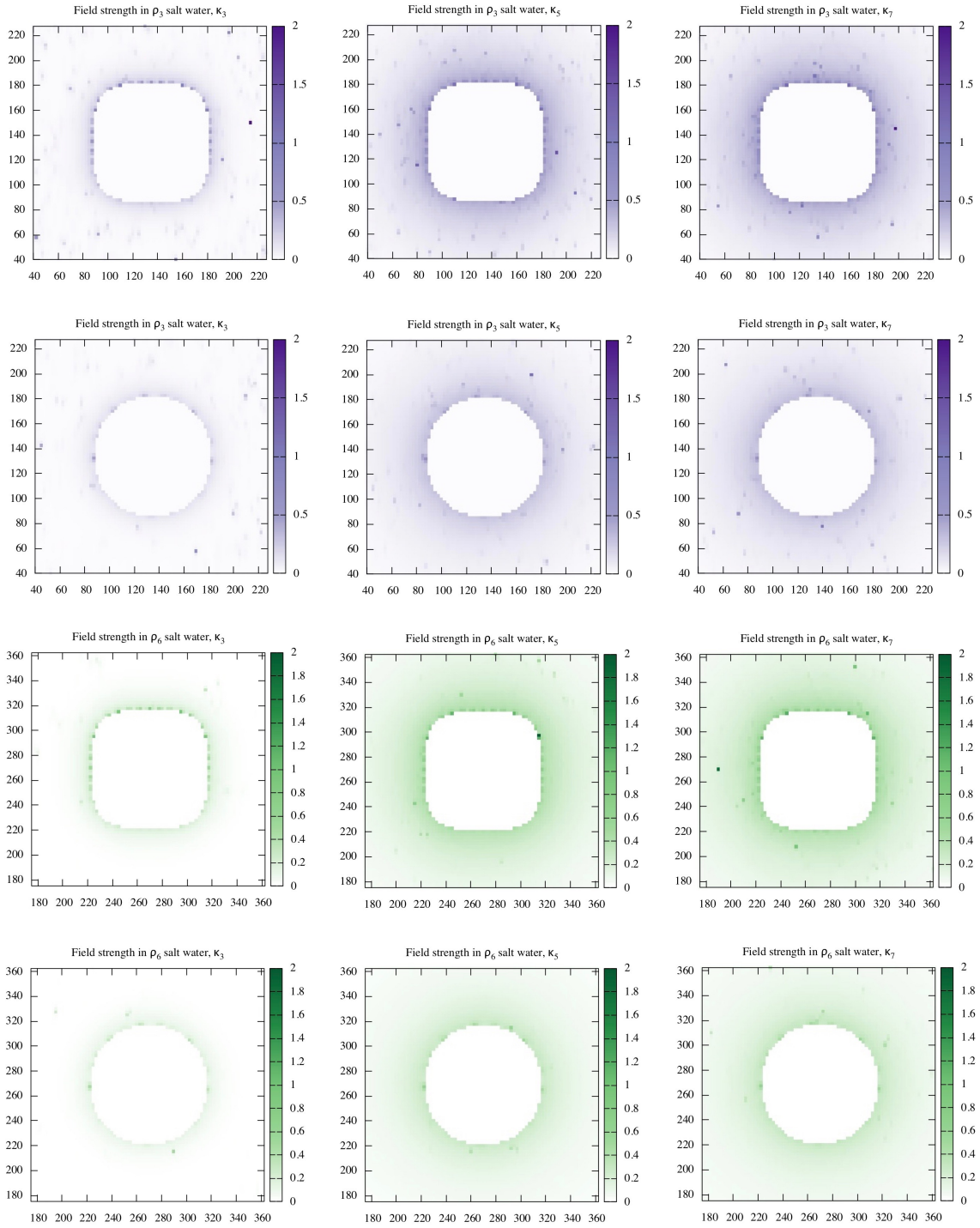

Figure 4.9: The strength of the electric field at varying salinities, as described by κ.

strength moving away from the surface is much sharper than in comparable spheres. We also see that in water, the differences in charge density affect the absolute value of the field strength, but not the shape of the layer. In ethanol, the change in charge density does not noticeably affect the field near the cube or sphere. Aside from the values extremely close to the surface of the colloid, the fields in ethanol also seem impervious to the shape of the colloid.

Moving to salinities, it is clear that at high ionic concentrations, the screening practically nullifies the field near the cube. This is not surprising, given the results shown in Figure 4.7 and Figure 4.8. We had hoped to be able to shed light on the differences between salinities of κ_5 and κ_7, but the distinction appears to be too fine for this style of visualization to adequately represent.

4.3 Conclusions

Overall, we have shown that variations in particle geometry, salinity and solvent affect the local electrostatic properties of the system. There are significant qualitative and quantitative differences between the electric double layer near different sections of colloid geometry for any solvent: these appear more pronounced in ethanol, the one solvent which does not see self-assembly. Increasing the ionic concentration of salt in the system leads to a breakdown in the electric double layer, which could potentially allow us to tune the affects of the anisometry on the self-assembly of the cubes. We also find that variations in the charge density conserve the qualitative electrostatic properties of the system, which will allow us greater flexibility in terms of simulation design for systems of multiple colloids.

5 | Pairwise interactions

Now that the first effects of the anisometry on the electrostatics have been established, we move to explain the assembly mechanism observed in experiment. This begins with a computer experiment to observe the self-assembly, followed by a series of simulations to measure the forces involved and compute the pair potentials at different orientations. By generalizing these results to different solvents and salinities, we see that we can move beyond merely understanding the assembly process to controlling it by tuneing the underlying electrostatic properties of the system.

5.1 Methods

Building on the methods explored in previous sections, the shift to multiple cube systems requires the addition of Van der Waals interactions and a system for cataloguing the mutual orientations of the cubes. For the former, we chose Hamaker constants as outlined in Section 3.1.3. The latter will be described here. We also discuss the specifics of calculating pair potentials based on simulation data.

5.1.1 Cube Orientations

5.1.1.a Quaternions

From a mathematical point of view, a quaternion is a 4-tupple (q_a, q_i, q_j, q_k) of real numbers. If we restrict ourselves to quaternions with norm one, we can identify them with the group of 3D rotations of an object in Euclidean space. In ESPResSo, the orientation of a particle can be set by defining its quaternion. This can be transferred into the more intuitive angle-axis representation by considering (q_i,q_j,q_k) as the unit vector representing the axis of rotation, and $\phi = 2\arctan 2(1, q_a)$[i]. as the rotation around this axis (in the mathematically positive sense). To give an example, we examine the cube pictured on the far left of Figure 5.1. We consider the orientation of the cubes with respect to the page, imagining the coordinate system given with the x axis along the width and the y-axis along the height, and see that it has undergone a rotation around the axis shown in black. This axis could be described by the vector $(0, 1, 0)$ in page coordinates, and and angle a. Then the corresponding unit quaternion can be computed by taking the tangens of the expression above, then normalizing the resulting quaternion $(q_a, 0, 1, 0)$ by dividing it by $\sqrt{q_a^2 + q_i^2 + q_j^2 + q_k^2}$. Due to

[i] the expression $\arctan 2(y, x)$ denotes the two-argument arctangent, which for $y = 1$ is defined by $\arctan 2(1, x) = \begin{cases} \arctan\left(x^{-1}\right) & \text{for } x > 0, \\ \pi/2 & \text{for } x = 0, \\ \arctan\left(x^{-1}\right) + \pi & \text{for } x < 0. \end{cases}$

the symmetry of the cubes, each orientation could be described by several different quaternions: we simply choose whichever one is most straightforward to calculate.

5.1.1.b Choice of Configurations Sampled

Now that we are able to represent the rotational configuration of the cubes, we can begin to consider how to systematically describe the different possible orientations. Since we will also strive to avoid re-sampling orientations that are equivalent due to symmetry, we begin by considering the three main symmetry axes of cubes as shown in Figure 5.1.

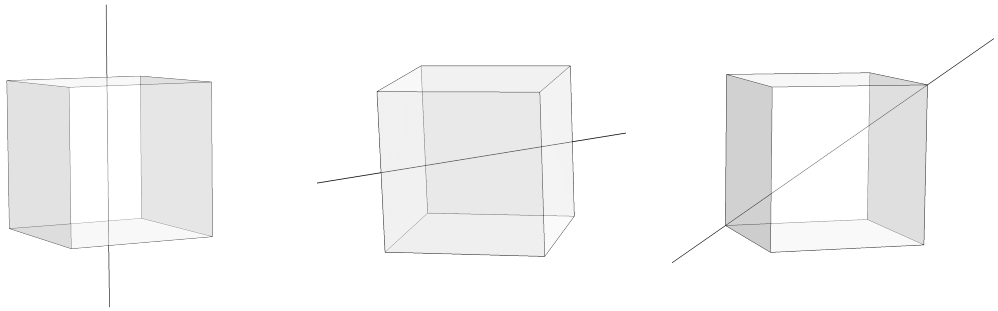

Figure 5.1: Sketch of the 3 different types of symmetry axes of a cube. Each cube has three four-fold symmetry axes through parallel cube faces, six two-fold symmetry axes through the centers of diagonally opposite edges, and four three-fold symmetry axes through diagonally opposite corners.

Brute-forcing this investigation to test all possible mutual orientations at all possible distances would mean sampling n angles × 3 axes × 2 cubes × m separations just for basic rotations without considering possible different heights. This may still sound reasonable until we consider that this is not the number of steps to be made, but the number of simulations that need to be run. Each configuration needs to be set, equilibrated, then integrated long enough that a sufficient amount of statistically independent measurements can be made. In order to move forward, we developed two different strategies to save computational effort:

Approach 1. Instead of trying to compute the key configurations for self-assembly, we simulated a two-cube system to see which orientations occur during an assembly process, then measured the potential for those configurations.

Approach 2. The list of computational demands above can be whittled down both by extended symmetry considerations to reduce the amount of configurations and simulation tricks to bring down the equilibration time. Since rotation around an n-fold axis of symmetry returns the cube to its original orientation after $360/n$ degrees, many angles need not be sampled. Moreover, since we do not care how the cubes are oriented with respect to the simulation box, the number of degrees above can be halved again for one of the cubes. As for the simulation speed ideas: these consisted of placing the counterions near the cubes based on the distributions obtained in Section 4.2 and

arranging the sequence of measurements so that the cubes only rotate or move very little between measurements.

While the second approach is mathematically satisfying, it still does not capture all orientations unless combinations of rotations are also considered, and doesn't include configurations where there is a height offset between the cubes (e.g. a face approaching a face at half height- cubes are always aligned through the x axis, without allowing for lateral movement). However, this method provides a framework to sample a representative amount of configurations, should such a depiction of the potential be called for.

5.1.2 Calculating the Pair Potential

As an MD simulations requires computing the force on the particles at each timestep, the additional step of intermittently outputting this force is cheap and straightforward. We can then perform the reverse of the calculation done in Section 2.2.1; namely, we obtain the pair potential U by integrating the force

$$\vec{\mathbf{F}} = -\boldsymbol{\nabla} U \ . \tag{5.1}$$

To put this into practice, we first note that, at fixed orientations, our pair potential U_q should only be a function of the distance r between the cubes. Although the force acting on the colloid is a 3 dimensional vector, we are only concerned with its projection onto the axis through the centers of both cubes i.e. the force acting in the direction of the approach. By aligning the direction of the approach of the cubes with x-axis, this projection becomes the x-component of the force vector, and so reduces Equation 5.1 to the one-dimensional case $f(x) = \frac{d}{dx} U_q(x)$.

Up until now, we have treated the force we obtain as if it were continuous. However, we can only measure a discrete set of force values. To perform the integration, we need to either fit the set of points with a (piecewise) integrable function or use a numeric approach. While the former should be simpler, it proved difficult to find a fitting function that could preserve the fine distinctions between different orientations without introducing oscillations due to the contributions of higher-degree polynomials. Instead, we integrate numerically by taking the average of the upper and lower Darboux sums. Let $u_q(x_k)$ let the value of the numeric approximation of the potential at x_k. This can be computed by

$$u_q(x_k) = \sum_{i=1}^{k} (x_i - x_{i-1}) \cdot \frac{f(x_i) + f(x_{i-1})}{2} \ . \tag{5.2}$$

This approach requires a fine spatial discretization $\Delta x = x_i - x_{i-1}$. However, we will see that only certain intercube distances are of interest. At extremely close distances, the steric potential adds an artificial repulsion, and at large enough separations the potential goes to zero. Since the discretization does not need to be uniform, we ran first set of measurements with large Δx (5nm)

over separation distances from 90 to 180nm, then re-ran a second set of simulations with smaller Δx (down to 2nm) in key areas.

5.1.3 System Setup

Two different kinds of simulations were run to obtain the results shown in this chapter. The first variant consisted of placing two cubes with their surrounding counterion clouds into a simulation box at a center to center distance lesser than two cube lengths, then equilibrating the system. This resulted in the cubes self-assembling, the mechanism of which could be observed in the trajectory files. To be able to quantify this process, a second type of simulation to measure the forces was run. These were carried out by fixing the cubes at specific distances and orientations, then equilibrating the system for this configuration and measuring the force between the two cubes. The trajectories of the cube assemblies lead us to focus our investigation on three key configurations (see Figure 5.2) which appeared essential to the assembly process.

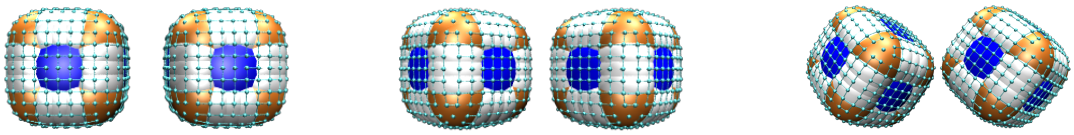

Figure 5.2: The three primary configurations investigated in this work. Each set of cubes shown at the same center to center distance of $120nm$.

Some preliminary simulations of intermediate configurations (e.g. corner to face) were also run, but all forces measured in these arrangements lay between those resulting from the configurations shown above. We also chose not to pursue the variation of charge densities, as the qualitative anisometry effects were shown to hold regardless of the concentration of counterions near the cube. Thus, a uniform charge density ρ_p was chosen based on the box length of 6σ. This is large enough to accommodate both cubes and their surrounding electric double layer even at separations greater than σ, while being small enough to remain computationally cheap to equilibrate. For two cubes, this gives $\rho_p = \frac{470 \cdot 2}{(6\sigma)^3} \approx 6 \cdot 10^{-6}$ without normalization by the number of charges, and ρ_6 as in Table 3.1.4 with the normalization by number of charges.

5.2 Results

As the data for this chapter coincided with the tail end of the tuneing process for the correct Hamaker constant strength, a multitude of tests were run in simulations with different charge densities, mass, size and interaction strength scalings and cube numbers (2 to 12). It also proved

interesting (albeit resource consuming) to run test simulations for pure Van der Waals and pure electrostatic repulsion to better distinguish the origin of different effects observed.

The data shown in this chapter was obtained from one simulation of the self-assembly type as described in the previous subsection, and two sets of pair potential measuring simulations for each of the water, ethanol and four salinities described in the subsequent section. The lowest salinity, $I_c = 10^{-7}$, was omitted since it has been showed to coincide with water. Each set of pair potential simulations equilibrated a system with two fixed cubes at a specific distance, then took 100 force measurements at intervals of 1000 integrations.

5.2.1 Self-Assembly of Cubes in Water

Simulations of cube pairs suspended in water showed a specific, persistent pattern in the way cubes approached each-other and assembled. The three main stages of the process are illustrated in Figure 5.3.

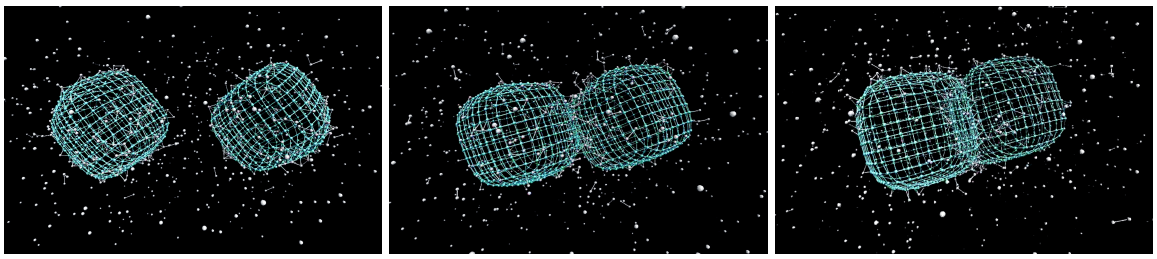

Figure 5.3: Two cubes (turquoise) surrounded by the counterions (gray) approach in a specific squence of mutual orientations, shown in chronological order from left to right.

At the beginning of the assembly process (left), cubes prefer to orient themselves corner to corner. Once the colloids are close, they rearrange into an edge to edge configuration (center). Finally, at equilibrium, they assume the orientation that maximizes the surface area in contact, which is a slightly off-center version of face to face. This assembly mechanism ties in to experimental observations that cubes appear to show a preference for corner to corner or edge to edge configurations during assembly, although only 2D images of the process exist, which make those two kinds of orientation hard to distinguish. In our investigation of the electric double layer, we saw that the screening of the face charges strongly differs from that near cube corners or edges.

To explain this process more systematically, we measured the forces as described in Section 5.1 and plotted the results in Figure 5.4. First, we see that despite the faces having the quantitatively highest counterion layer, their configuration does not become favorable until the cubes are so close that other orientations being to encounter steric repulsion. This may seem counterintuitive, but make sense in the light that faces have a far greater surface area (and so more charges) at closer proximity to each other compared to, for instance, a corner to corner configuration at the same surface-to-surface distance. Considering that, it is almost surprising that the gap between

the amount of counterions near surfaces as opposed to corners and edges is not more pronounced. Indeed, this configuration only occurs when the Van der Waals attraction is close to its maximum. The slight angle between assembled cube pairs has also been seen in experiment, most notably in lattices formed by such cubes[31].

In contrast, the edge to edge configuration only appears to be favorable within a short (around 15nm) range of distances, although it is only slightly less attractive than the corner to corner configuration at greater distances. This could be explained by the strong distance dependence of the Van der Waals attraction. Since the difference in screening between corners and edges is not as pronounced, cubes initially prefer the configuration with the lowest electrostatic repulsion. Once they draw closer, the Van der Waals attraction grows and can overcome the electrostatic repulsion of the edges, despite them being less well screened than the corners.

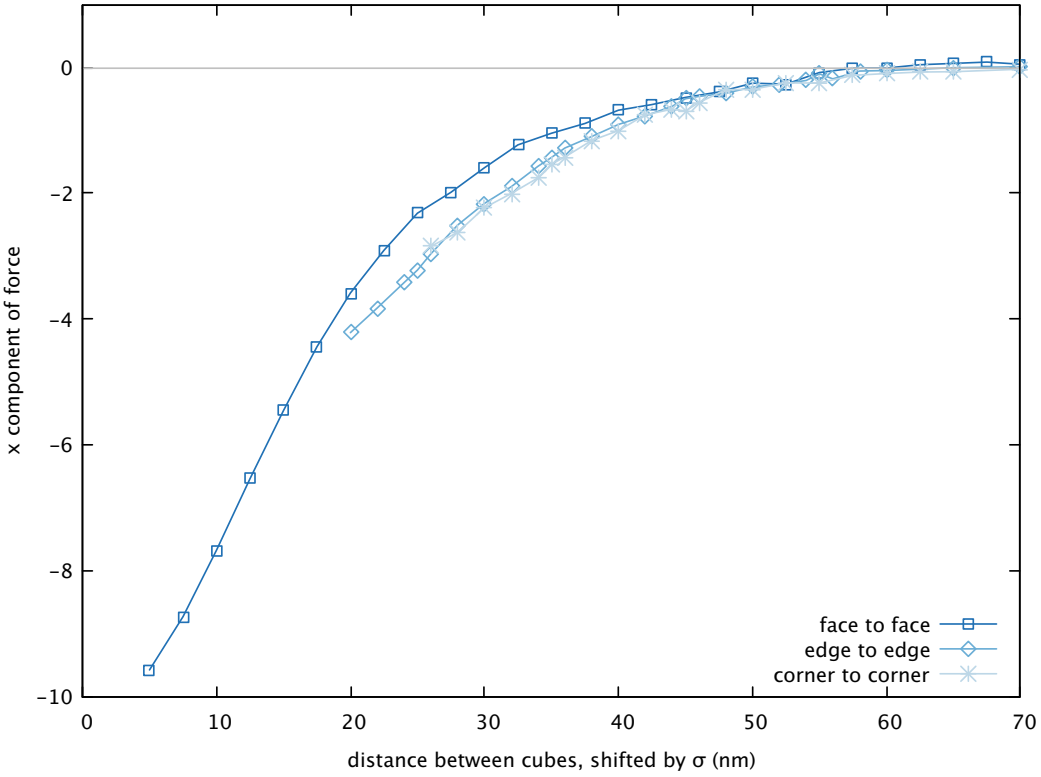

Figure 5.4: The force acting on a cube at specific distances and orientations from another cube. Although the distances were measured from center to center of the colloids, they are shifted by subtracting σ so that 0 represents the surface contact distance for the face to face orientation. Edges would touch at just under 20nm, and corners at around 25nm in this scaling.

Although the corner to corner configuration does not appear to be significantly more favorable that that of edge to edge, it is consistently seen in two-cube assemblies. This may, however, partially be due to one of the modelling assumptions: the grid created in Section 3.1.1.a specifically places

charges on the "corner" of the colloids, which are pointed directly at each other due to the alignment of the cubes along the three-fold symmetry axes. If once considers the corner to corner configuration in Figure 5.3 closely, it's possible to see that the corners are not precisely in line- the cube on the left is tilted slightly towards the reader and down, while the cube on the right is tilted up. In that vein, one should also note that while the overall charge density was matched to experiment, the charges in the corners are slightly closer to each-other due to the curvature of the superball (see for instance Figure 5.2). The reasoning behind these modelling choices was that, given the experimental guidance that cubes may prefer corner to corner configurations, care should taken to not bias the model in favor of such alignments, as might occur if charges were removed from the corners to "correct" the charge densities. Before moving to the pair potential, we also note that thermal fluctuations will still affect the cubes at any distance, creating noise which averaged out over a sufficient number of input configurations.

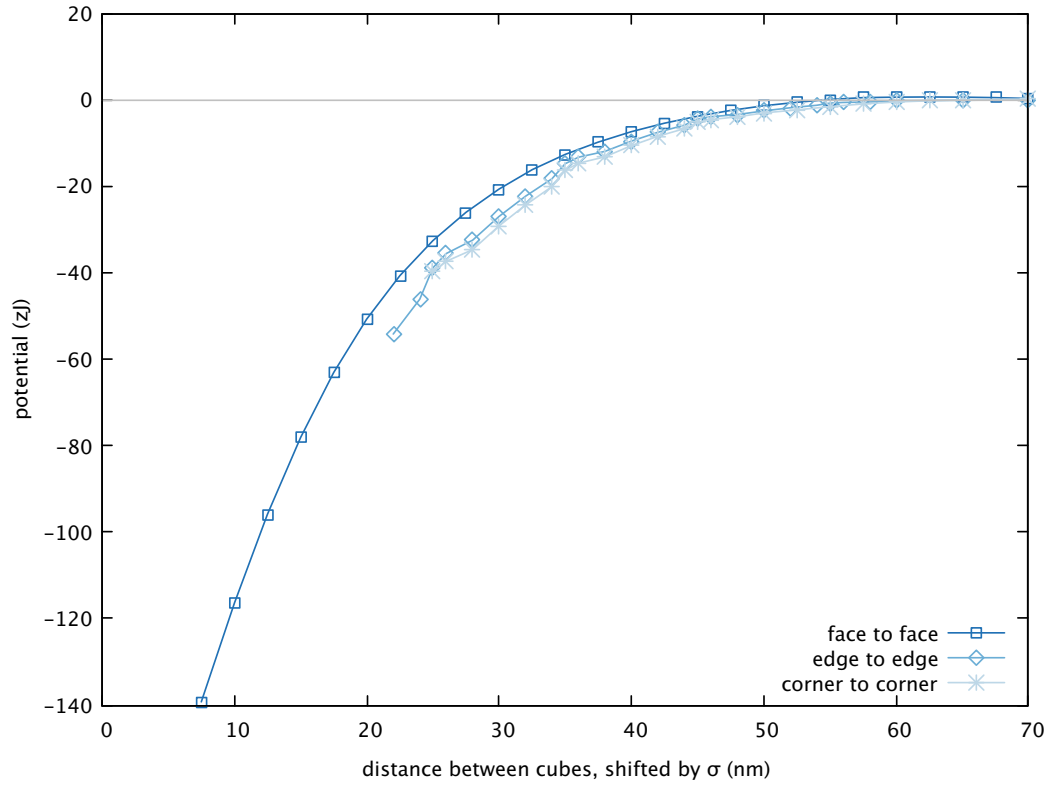

Figure 5.5: Pair potential of cubes in water. The same distance conventions apply as in Figure 5.4.

Using numerical integration, we obtained the pair potential shown in Figure 5.5. This formalizes our discussions regarding the favorability of certain orientations; moreover, we now have specific values for the potential to compare to experimental and/or analytical results for similar systems. As the distance between the cubes decreases, decreases to well below $100zJ$, which

makes the cube clusters very stable at room temperature. In the limits of larger separations, we see that the interaction potential goes to zero.

As previously mentioned, the difference between the values of the potential for the three mutual orientations concur with the preferences of cube assemblies to favor edge to edge or corner to corner configurations. However, the quantitative differences in attraction at different orientations appear less pronounced than expected. This may be a kinetic effect stemming from the lack of hydrodynamics in simulation. In the current model, translational inertia is completely isotropic, meaning that a cube moving forward face first receives the same energetic penalties as a cube moving in the direction of an edge or corner. Although it is intuitively obvious that a cube face moving forward would be less favorable than the other configurations, the flow around a moving cube is non-trivial to estimate and would require further study.

Comparing to the standard DLVO-curves as shown in Figure 2.3, we find our curves closely resemble those shown for very low σ. We do not see a secondary minimum and energy barrier structure, presumably due to the low charge density. We also note that the double layer repulsion, at least in the face to face configuration, will not necessarily follow the $\frac{1}{r^2}$ curve of the isotropic case depicted in such textbooks.

5.2.2 Colloidal Stability in Ethanol

Experiments showed that the cubes do not self-assemble in ethanol[1]. This provided an opportunity to test the calibration of the attractive interactions. After a first round of measurements and averaging, as shown in Figure 5.6, we see that the results (points) are far noisier than in the previous case. Aside from a few data points in the face to face interaction series at very close range, the values fluctuate around zero. To check for an overall trend in the measurements, we used gnuplot's implementation of the Levenberg-Marquardt algorithm to attempt a least squares fit of the data to a linear function.

Configuration	Slope	Intercept	Root-mean-squared error
face to face	0.0186479	-2.75425	0.328068
edge to edge	0.00934946	-1.3856	0.161957
corner to corner	0.00666777	-0.965225	0.162383

Table 5.1: Fitting parameters of a least squares fit of the data to a linear function.

While small in absolute terms, the RMS is significant compared to the values of the data. To obtain a more rigorous result would require finding a way to clean up the input data, e.g. taking more measurements to attempt to reduce the noise in the input data. However, given the original concept of using these measurements as a quick sanity check, it does not appear expedient to pursue the matter further. We see that the behavior of the cubes in ethanol matches the stability

observed in experiment, and the fitted lines confirm that there is no significant overall trend. While the forces could be slightly attractive at the separation where the Van der Waals interaction reaches its peak, this attraction would at most reach the order of the thermal fluctuations in the system. We also see that the attraction strength chosen is presumably near the upper end of the range of realistic values.

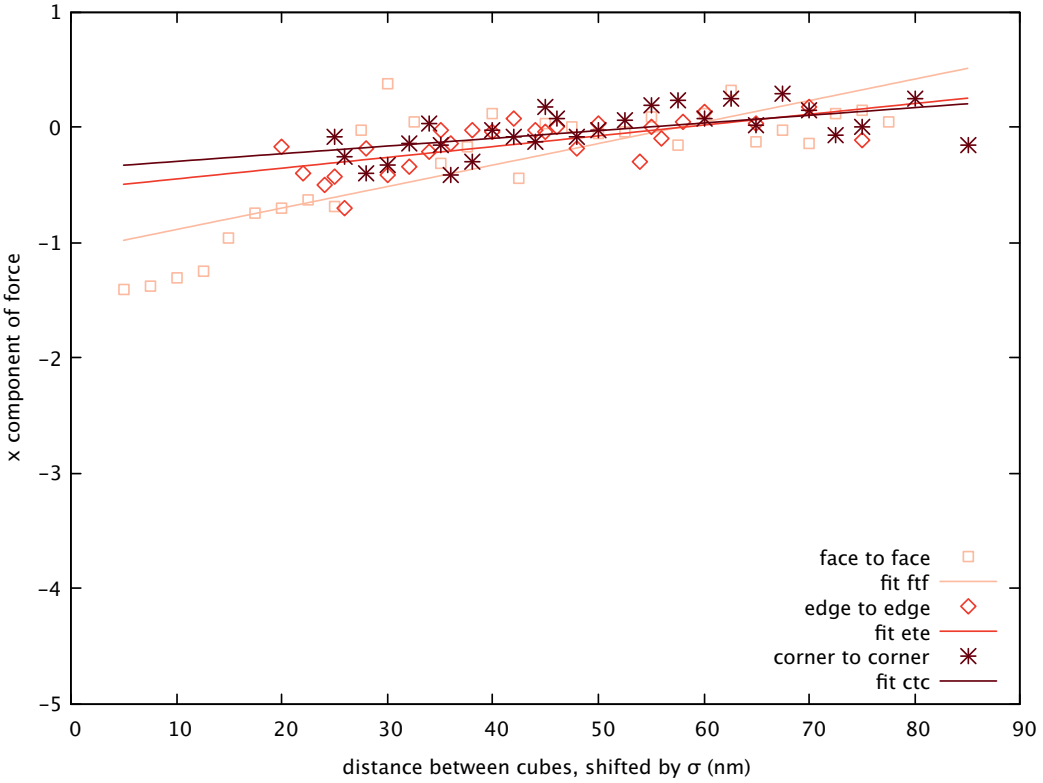

Figure 5.6: The force exerted by a cube on another cube in ethanol. The same distance conventions with respect to the x-axis apply as in Figure 5.5, although the y-axis is scaled differently to allow some distinction between the different points. The linear fittings show that, overall, there is no significant trend in the measurements. Only the face to face configuration shows a little attraction at very close range.

5.2.3 Effects of Varying Salinity

After studying the effect of the solvent, we move to varying the salinity of the solution. Since the difference between the salinities is subtle, we will only show the highest ($I = 10^{-3}$) and lowest ($I_c = 10^{-6}$) used. In Figure 5.7, we see the pair potential at different orientations for those salinities. For low salinities (bottom graph), the potential is practically identical to the salt-free case. Since the Debye lengths for concentrations below 10^{-5} molar are greater than the separation distances at which the potential is measured (see Table 3.1.1.c), it does not noticeably affect the colloids aside from slight differences in the density profiles. But this does not suffice to affect the overall

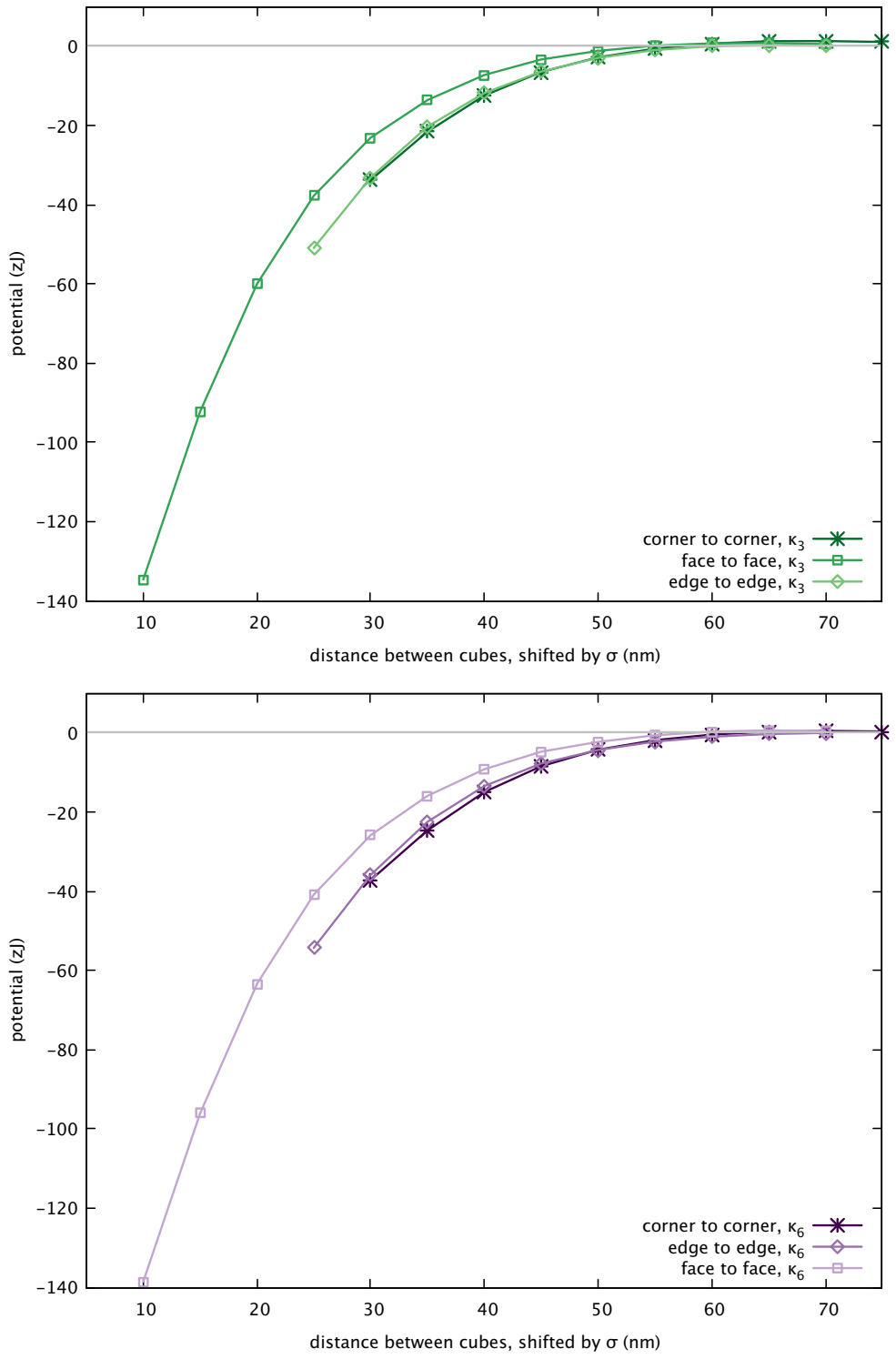

Figure 5.7: Pair potentials at ionic concentrations of $I = 10^{-3}$ (top, green) and $I = 10^{-6}$ (bottom, violet). The same distance conventions apply as in Figure 5.5.

potential. In contrast, once the salinity is high enough for the electric double layer to break down, the potential becomes slightly less attractive at close ranges and the anisometry effects begin to disappear. The former is counter-intuitive, but can be explained by the fact that at close distances, the screening due to the increased salt content is not as strong as the screening provided by the electric double layer in other systems. While examining the differences in the double layer contingent on the geometric feature of the colloid directly beneath it (see Figure 4.7), we saw that the differences in double layer near edges and corners were minimal, despite edges having comparatively more charges at a lesser distance from the edge. This may suggest that the corner to corner approach was energetically favorable because their repulsion was more strongly screened. Without an electric double layer, the screening is independent of the colloid's shape. This would explain why the corner to corner and edge to edge configurations no longer differ energetically, although the face to face configuration is still more repulsive. This suggests that, although the anisometry's effect on the distribution of ions can be tuned by changing the salinity, there is no experimentally attainable salt concentration at which the pair potential becomes independent of cube orientations. In Figure 5.8, we show the direct comparison between high and low salinity for two configurations.

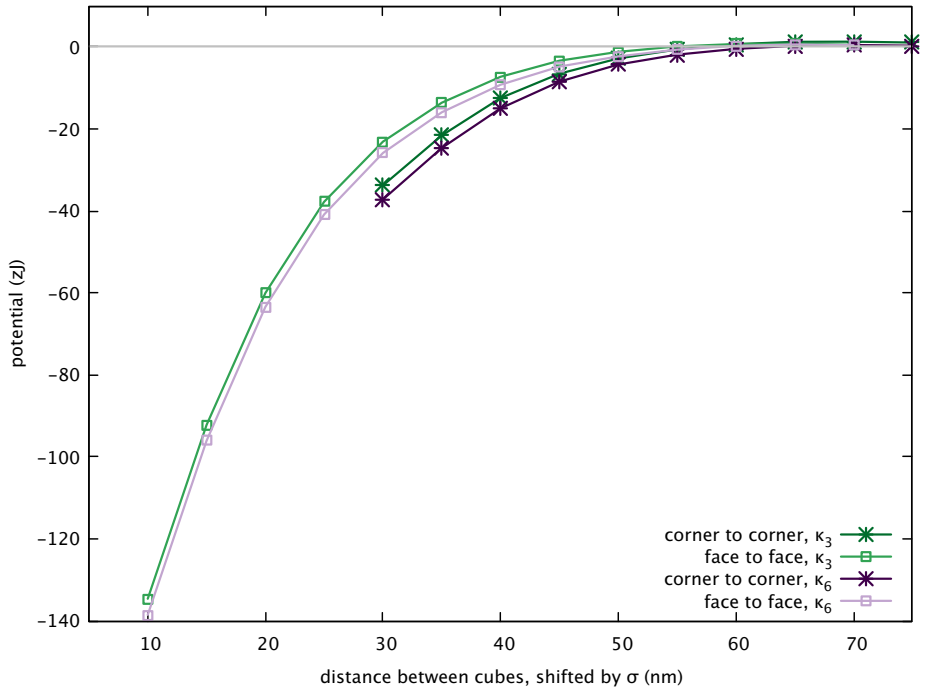

Figure 5.8: This plot combines the face-to-face and corner-to-corner pair potentials of Figure 5.6 to show the effect of the difference in ionic concentration more clearly. The edge to edge configurations were omitted, since they partially overlap with the corner to corner configurations.

These potentials show a pronounced gap between different salinities, which slowly decreases

as the potential goes to zero. Since the difference in terms of absolute value was not very large, the intermediate salinities were not evaluated. Overall, differences in the ionic concentration of salt in the solvent do not show a strong affect on the interaction potential of cubes, except in the (experimental) limit cases.

5.3 Conclusions

Our simulations were able to verify that the experiment-based hypothesis of charged cubes having a specific self-assembly pattern, in which edges in corners play a decisive role. The pair potential of these colloids is strongly affected by their mutual orientation. Although the choice of attraction strength cannot be entirely founded in experiment, we are able to obtain realistic values of the potential. The model can be extended to produce results in ethanol, which shows the expected colloidal stability. Changing the ionic concentration of salt in the solvent has a clear influence on the potential, though the effect would not fundamentally change the behavior of the system and requires increase or decrease in salt concentration of several orders of magnitude to be noticeable.

6 | Outlook

This thesis presented a primer on mechanism of cube self-assembly, and the factors pertinent to alter or prevent it. Depending on the desired outcome, there are several starting points for further study. For instance, one could tune the shape of the superball to study the transition from the pronounced non-uniform distribution of counterions in the electric double layer of a cube to the symmetry found in the layer surrounding a sphere. Given that the shape of the pair potentials appears close to that predicted by DLVO theory, albeit only for fixed orientations, increasing the charge density on the surface of the colloids could also lead to a different potential shape. To make the results more precise, one could modify the standard Lennard-Jones potential to include the additional Van der Waals attraction terms discussed in the theory section. One could also test decreasing the attraction strength, since simulations indicate the initial estimates may near the upper end of the realistic range. To explain why the anisometry effects are so pronounced despite the modest difference the values of the attractive potential at different orientations, it would be interesting to include some hydrodynamics.

Moving towards matters of interest for potential applications, the logical next step would be to study the assembly of cubes in bulk and the resulting microstructures. This will face computational constraints due to the timescales involved, and since collecting enough data on a system undergoing an irreversible process to ensure independence of the results from the initial conditions will be challenging. Some tests have already been run, hinting at familiar preferences in attachment and showing strongly anisotropic microstructures.

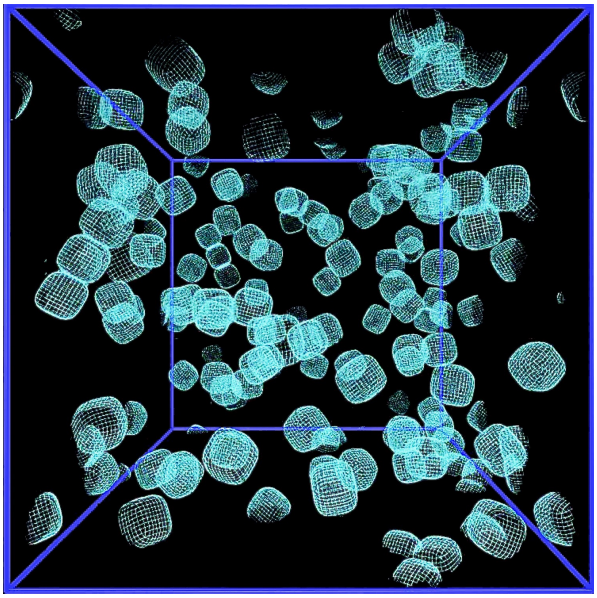

Figure 6.1: Bulk simulation of cubes in water. The system has not yet reached equilibrium, but we already see that several chains (left, center) and a small cluster (right) have formed.

7 | Appendices

7.1 Experimental Parameters

In addition to the values cited in literature, the sketch and images of superballs in Figure 7.1 was provided to serve as basis for the cube model.

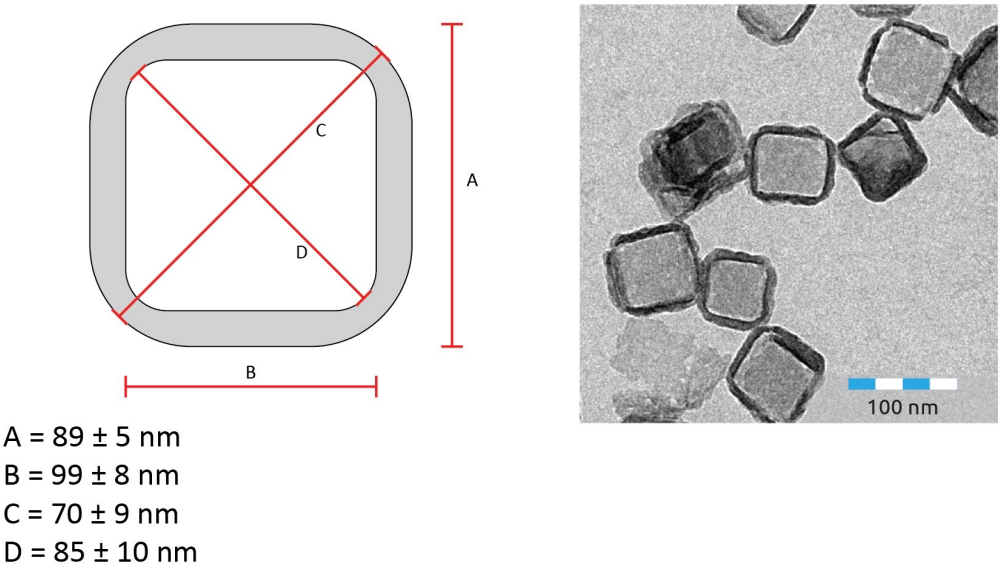

Figure 7.1: Sketch and image of cubes provided by F. Dekker, A.P. Philipse.

The following parameters were provided by our experimental partners (σ, I,ρ) or estimated based on the sketch above (q, σ_c):

Symbol	Name	Value
q	superball shape parameter	1.7
σ_c	diameter of cubes	90 nm
σ	surface charge density	$5\text{-}10 \cdot 10^{-3}$ per nm^2
I	ionic concentration	$10^{-7} - 10^{-3}$ molar
ρ_S	density of silica	$1.5 - 1.8$ g/mL

Table 7.1: Table of experimental parameters.

References

[1] FRANS DEKKER, REMCO TUINIER and ALBERT P. PHILIPSE. *Colloids and Interfaces*, **2**, (2018).

[2] JOE G. DONALDSON, ELENA S. PYANZINA and SOFIA S. KANTOROVICH. *ACS Nano*, **11** PMID: 28763187, 8153–8166, (2017).

[3] JOEN J. HERMANS. *Cluster formation in deionized dispersions of hollow silica cubes*. Master's Thesis. 2012.

[4] A. D. MCNAUGHT and A.WILKINSON. *Compendium of Chemical Terminology, 2nd ed.* 1997.

[5] E. MATIJEVIC. *Medical Applications of Colloids*. Springer, 2008.

[6] RAFFAELE MEZZENGA, PETER SCHURTENBERGER, ADAM BURBIDGE and MARTIN MICHEL. *Nature materials*, **4**, 729–40, (2005).

[7] RENÉ VAN ROIJ, MARJOLEIN DIJKSTRA and JEAN-PIERRE HANSEN. *Phys. Rev. E*, **59**, 2010–2025, (1999).

[8] JEAN-MARC VICTOR and JEAN-PIERRE HANSEN. *J. Chem. Soc., Faraday Trans. 2*, **81**, 43–61, (1985).

[9] LAURA ROSSI, STEFANO SACANNA, WILLIAM T. M. IRVINE, PAUL M. CHAIKIN, DAVID J. PINE and ALBERT P. PHILIPSE. *Soft Matter*, **7**, 4139–4142, (2011).

[10] LAURA ROSSI, VISHAL SONI, DOUGLAS J. ASHTON, DAVID J. PINE, ALBERT P. PHILIPSE, PAUL M. CHAIKIN, MARJOLEIN DIJKSTRA, STEFANO SACANNA and WILLIAM T. M. IRVINE. *Proceedings of the National Academy of Sciences*, **112**, 5286–5290, (2015).

[11] ROBERT D. BATTEN, FRANK H. STILLINGER and SALVATORE TORQUATO. *Phys. Rev. E*, **81**, 061105, (2010).

[12] J. M. MEIJER. *Colloidal Crystals of Spheres and Cubes in Real and Reciprocal Space*. Doctoral Thesis. Utrecht University, 2015.

[13] JACOB N. ISRAELACHVILI. *Intermolecular and Surface Forces*. Third Edition San Diego: Academic Press, 2011.

[14] JANNE-MIEKE MEIJER, ANTARA PAL, SAMIA OUHAJJI, HENK N. W. LEKKERKERKER, ALBERT P. PHILIPSE and ANDREI V. PETUKHOV. *Nature Communications*, (2017).

[15] V. ADRIAN PARSEGIAN. *Van der Waals Forces: A Handbook for Biologists, Chemists, Engineers, and Physicists*. Cambridge University Press, 2005.

[16] M. KLEMAN, O.D. LAVERNTOVICH, J. FRIEDEL and O.D. LAVRENTOVICH. *Soft Matter Physics: An Introduction*. Partially Ordered Systems Springer, 2003.

[17] H.C. HAMAKER. *Physica*, **4**, 1058–1072, (1937).

[18] FABIO L. LEITE, CAROLINA C. BUENO, ALESSANDRA L. DA RÓZ, ERVINO C. ZIEMATH and OSVALDO N. OLIVEIRA. *International Journal of Molecular Sciences*, **13**, 12773–12856, (2012).

[19] P. DEBYE and E. HUECKEL. *Physikalische Zeitschrift*, (1923).

[20] DAAN FRENKEL and BEREND SMIT. *Understanding Molecular Simulation (Second Edition)*. Second Edition San Diego: Academic Press, 2002. 589–617

[21] M. P. ALLEN and D. J. TILDESLEY. *Computer Simulation of Liquids*. New York, NY, USA: Clarendon Press, 1989.

[22] JOE G. DONALDSON. *Colloidal Magnetic Cubes*. Doctoral Thesis. University of Vienna, 2018.

[23] PAUL LANGEVIN. *C. R. Acad. Sci. Paris*, (1908).

[24] L.D. LANDAU and E.M. LIFSHITZ. ed. by L.D. LANDAU and E.M. LIFSHITZ Third Edition Oxford: Butterworth-Heinemann, 1980. 333–400

[25] GARY S. GREST and KURT KREMER'. *Physical Review A*, **33**, (1986).

[26] AXEL ARNOLD, OLAF LENZ, STEFAN KESSELHEIM, RUDOLF WEEBER, FLORIAN FAHRENBERGER, DOMINIC ROEHM, PETER KOŠOVAN and CHRISTIAN HOLM. 'ESPResSo 3.1: Molecular Dynamics Software for Coarse-Grained Models' in: *Meshfree Methods for Partial Differential Equations VI*. ed. by MICHAEL GRIEBEL and MARC ALEXANDER SCHWEITZER Berlin, Heidelberg: Springer Berlin Heidelberg, 2013. 1–23

[27] JOE G. DONALDSON, PER LINSE and SOFIA S. KANTOROVICH. *Nanoscale*, **9**, 6448–6462, (2017).

[28] ÁLVARO GONZÁLEZ. *Mathematical Geosciences*, **42**, 49, (2009).

[29] M. MOHSEN-NIA, H. AMIRI and B. JAZI. *Journal of Solution Chemistry*, **39**, 701–708, (2010).

[30] JOHN R. TAYLOR. *Classical Mechanics*. 2005.

[31] JANNE-MIEKE MEIJER, FABIAN HAGEMANS, LAURA ROSSI, DMYTRO V. BYELOV, SONJA I.R. CASTILLO, ANATOLY SNIGIREV, IRINA SNIGIREVA, ALBERT P. PHILIPSE and ANDREI V. PETUKHOV. *Langumuir*, (2012).